DALHOUSIE UNIVERSITY

Micro-petrological Analysis of Shergottite Meteorite North West Africa 4468

Galena Roots

SUBMITTED IN PARTIAL FULFILLMENT OF THE REQUIREMENTS FOR
THE DEGREE OF BACHELOR OF SCIENCES, HONOURS
DEPARTMENT OF EARTH SCIENCES
DALHOUSIE UNIVERSITY, HALIFAX, NOVA SCOTIA

April 2019

DALHOUSIE UNIVERSITY

DATE: 28 April 2017

AUTHOR: Galena Roots

TITLE: Micro-petrological Analysis of Shergottite Meteorite North West Africa 468

Degree: B. Sc. Honours Earth Sciences Convocation: May Year: 2017

April 2019

Distribution License

DalSpace requires agreement to this non-exclusive distribution license before your item can appear on DalSpace.

NON-EXCLUSIVE DISTRIBUTION LICENSE

You (the author(s) or copyright owner) grant to Dalhousie University the non-exclusive right to reproduce and distribute your submission worldwide in any medium.

You agree that Dalhousie University may, without changing the content, reformat the submission for the purpose of preservation.

You also agree that Dalhousie University may keep more than one copy of this submission for purposes of security, back-up and preservation.

You agree that the submission is your original work, and that you have the right to grant the rights contained in this license. You also agree that your submission does not, to the best of your knowledge, infringe upon anyone's copyright.

If the submission contains material for which you do not hold copyright, you agree that you have obtained the unrestricted permission of the copyright owner to grant Dalhousie University the rights required by this license, and that such third-party owned material is clearly identified and acknowledged within the text or content of the submission.

If the submission is based upon work that has been sponsored or supported by an agency or organization other than Dalhousie University, you assert that you have fulfilled any right of review or other obligations required by such contract or agreement.

Dalhousie University will clearly identify your name(s) as the author(s) or owner(s) of the submission, and will not make any alteration to the content of the files that you have submitted.

If you have questions regarding this license please contact the repository manager at dalspace@dal.ca.

Grant the distribution license by signing and dating below.

_____ _____

Name of signatory Date

Table of Contents

Table of Figures

Abstract

This study investigates the chemical variations within mineral phases in the Martian meteorite sample North West Africa (NWA) 4468. Meteorites are the only samples of Martian rocks that can be studied directly. Their geochemical and mineralogical compositions provide key evidence for magmatic processes occurring on Mars. Recent observations of volcanic areas on Mars, e.g. the Athabasca Valles, suggest that Mars is in fact still a volcanically active planet. Application of micro-petrology, i.e. processes represented and recorded on a mineral-scale, is the only effective way to study meteorites which are exceedingly rare and found only as very small volume samples. Meteorite NWA 4468 is an example of a Shergottite, a group of 150-220 Ma Martian meteorites, typically basaltic in composition, coarse grained and enriched in incompatible elements. NWA 4468 is a basaltic sample with large pyroxene oikocrysts, olivines, oxides and plagioclase grains. The later have been shock-altered to maskelynite. Shergottites are generally thought to represent cumulates fractionated from high-volume melting of the lower, primitive, Martian mantle. Samples were examined using reflected light microscopy and back-scattering electron-imaging, followed by detailed X-ray mapping of both the large olivine and pyroxenes crystals. The olivine crystals are generally not zoned in Fe and Mg, but do preserve phosphorus zoning. This occurs in about 20% of the olivine crystals and suggests early skeletal growth and subsequent ripening of the crystals, which in turn overprinted any Fe and Mg zoning that may have originally occurred. This type of P-zoning has been noted in terrestrial basaltic samples and can used to make predictions about the growth history and cooling rates recorded. In this case the olivine crystals formed early in the crystallization history but also at elevated temperatures. Pyroxene oikocrysts show distinct zoning from pigeonite to augite, i.e. from Ca-rich and Ca-poor sectors within individual grains. Zoning in Fe and Mg is also partially preserved in the pyroxene crystals. This can be used to determine the minimum recorded crystallization temperatures and relative cooling rates. The pyroxene crystals in this example likely formed later and at cooler temperatures than the olivine crystals. Analyses of oxides and have also been carried out to enable as wide a range of mineral thermobarometers as possible to be applied. Applied thermometry and barometry, combined with characterization of preserved micro-textural features in NWA4468, will provide further insight into the overall formation of large magmatic systems on Mars.

Key Words: Shergottite Northwest Africa 4468, Geochemistry, Crystallization. Magmatism, Mars, Phosphorous zoning

Acknowledgements

I would like to thank Richard Cox for supervising this project and for all this, for his knowledge, time and patience. Thank you to SELF for their generous funding making the La-ICP-MS and EMP work possible. Thank you to the Dan MacDonald for all his help with the microprobe analyses, Erin Keltie at the LA-ICP-MS lab and Djordje Grujic for coordinating the honours course.

Thank you to the faculty and staff in the Dalhousie Earth Science Department for all that you have taught me about geology and academia, as well as the opportunities and memories that you have given me. Special thanks to my friends at Dalhousie and family for their encouragement throughout the process of this project.

Chapter 1: Introduction

Geochemical data is often used in the study of mafic magmas to model cooling histories and subsurface magma processes. This is done by comparing variations in mineral textures and mineral compositions within a suite of rocks. The application of these methods on a micro-textural and chemical scale is useful in both the analysis of terrestrial rocks and is essential to understanding the formation histories of meteorite samples. The knowledge of Martian geology is increasing rapidly due advancements in technologies which are allowing for more in depth studies of Mars's surface and the understanding of its meteorites. Martian data collection can only be obtained by remote sensing satellite imagery, in-situ rover analysis and direct observations of Martian meteorites. Micro-petrology is the only effective ways to study meteorites which are exceedingly rare and found only as very small volume samples. This study investigates the geochemical variations within mineral phases in the Martian meteorite sample North West Africa (NWA) 4468 with the goal of determining the samples goethermometry. Comparing the geothermometery and preserved mineral micro-textures of NWA 4468 with similar information of other meteorites aids in the understanding of the cooling history of this sample.

Chapter 2: Geological Setting

2.1 Area of Study

The developing understanding of Martian geology has been the result of space craft remote sensing, in situ rovers studies and meteorite analysis. Although Martian meteorites have similar mineral compositions to terrestrial rocks, they have a higher Fe/Mg ratios within pyroxenes, distinct oxygen isotopic compositions and can have Martian atmospheric gas trapped within glass (McSween, 1985). Shock alterations are also observed on both a hand sample and mineralogical scale in all meteorites. Shock alteration features include fission crusts and shock altered plagioclase to maskylonite. Martian rocks can be distinguished from other extra-terrestrial (Lunar achondrite and other achondrites) rocks by their lower Fe/Mn ratios in pyroxene and olivines (McSween, 1985). McSween and Treiman (1998) classified Martian meteorites by their mineral composition into three distinct categories Chassignite (dunites), Nakhlites (pyroxenites) and Shergottites. Shergottites were further classified into basaltic, olivine-phyric and Iherzolitic/poikilitic compositions (Goodrich, 2002).

The composition of Martian rocks gives an idea of what geological process the plant has undergone but to fully understand the plants geology, it is important to know what changes the plant has undergone over time. The timing of planetary geological processes is strongly dependent on the analysis of crater densities. The number of accumulated craters on a planetary surface can be used to determine age constraints for erosional and heightened volcanic periods (Stoffler and Ryder, 2001). Despite the potential errors associated with using this chronological technique (Lissauer et al. 1988), distinct changes can be observed throughout Martian history. High crater densities define the Noachian epoch (before 3.5 Gyr) (Tanaka et al. 1987). The Hesperian (3.5 to ~3.0 Gyr) shows active volcanic and fluvial processes as well as rapid periglacial resurfacing rates (Tanaka et al. 1987). Since ~3.0 Gyr Mars has been in the Amazonian epoch, which has been tectonically quiet except for the presence of upper Amazonian volcanic features (300 Myr ago) (Hartmann and Neukum, 2001). Radiometeric dating technics are used to date crystallization ages of meteorites which in combination with crater density dating helps to confine ages of geological processes on Mars.

2.2 Previous work

NWA 4468 is a 675g Martian meteorite that was discovered in the Western Sahara desert of Morocco in 2006, and classified as a basaltic shergottite with large orthopyroxene oikocrysts and olivine chadacrysts by Irving et al. (2007). The sample is determined to be 35% olivine, 30% pyroxene, 25% masklynite and contains Ti-chromite, ilmenite, merrillite, Cl-apatite and pyrrhotite (Irving et al., 2007) crystals. NWA 4468 also has large orthopyroxene oikocrysts (2-10mm across) enclosing chadacrysts of Ti-poor chromite and olivine (Irving et al. 2007). The sample, in common with most Shergottites, is enriched in incompatible trace elements and has a flat REE pattern (Borg et al. 2008). NWA 4468 differs from most other enriched shergottites due to its orthopyroxene oikocryst and it not being a olivine-phyric (Irving et al., 2007).

Previous studies determined the ages of NWA 4468 to be 179 $\pm$ 27 Ma (Lapen et. al 2009), 187 $\pm$ 6Ma(Marks et al., 2010) and 150$\pm$29 Ma (Borg et al 2008) determined by Lu-Hf, Rb-Sm and Sm-Nd dating techniques respectively. Given the margin of error within each of these dating techniques NWA4468 is similar in age to other enriched shergottites such as NWA 1068, that range from 165 Myr (Rb-Sr age of Shergotty (Nyquist et al 1979, Bouvier et al. 2008)) to 207 Myr (Rb-Sr age of LAR 06319 (Shih et al. 2009; Shafer et al., 2010)). These enriched Shergottites are all of Late Amazonian age (< 230 Myr (Hartmann, 2005). During this time period (2 Myr – 250 Myr) local volcanism was prominent, which created large shield volcanos and extensive basalt flows. Vaucher et al. (2009) estimated the volume of lavas to be 1.3 e^5 – 1.7 e^5 km^3, which suggests that volcanic activity occurred for about 300 Myr resulting in large shield volcanoes.

NWA 4468 has a similar mineral and whole rock composition to olivine-shergottite, LAR 06319 and NWA 1068, as well as flat and elevated rare earth element patterns which are rare in enriched shergottites. (Sarbadhikari et al., 2009). Marks et al. (2010) used the elemental compositions of NWA 4468 to determine potential similarities between it and other iron-rich, incompatible element-rich Martian meteorites. The volcanism study modeled a crystallization path (Fig. 1) that suggests a parent melt composition which would have been similar to that of NWA 4468, fractionation this melt produced compositions similar to that of other shergottite

meteorites such as LA1, Shergotty and Dho 376 (Marks et al. 2010). This study also found that a similar trend may have been produced using NWA1068 as the parent composition, with the dominant process being fractional crystallization producing other Shergottites (Marks et al. 2010). The removal of plagioclase from the composition of NWA 4468 results in a similar composition as that of NWA 1068, the similarity in this compositions suggests that NWA 1068 could be related to NWA 4468 with the removal of plagioclase by crystallization fractionation (Symes et al. 2008). Furthermore, the fractional crystallization of NWA 4468 removed olivine which relates NWA 4468 to LA1.

Filiberto (2017) determined the average mantle potential temperature, which is defined as "the temperature the mantle would have at the surface, if it ascended along an adiabat without undergoing melting" (Mckenzie and Bikle, 1988), for Ol-phyric shergottites to be 1745 $\pm$ 40 °C which is hotter than the potential temperature of the older Noachian mantle which is ~1450 °C. The temperature of formation in these meteorites was calculated using Mg-exchange and was determined to range from 1630 (DaG 4467/489) to 1736 (Tissint) (Filiberto, 2017). Silica-activity barometer determined Ol-phyric shergottites pressures range from 2.3 GPa (NWA 5789) to 6.2 GPa (NWA 6234) (Filiberto, 2017). All the calculations were done assuming a volatile-free mantle source.

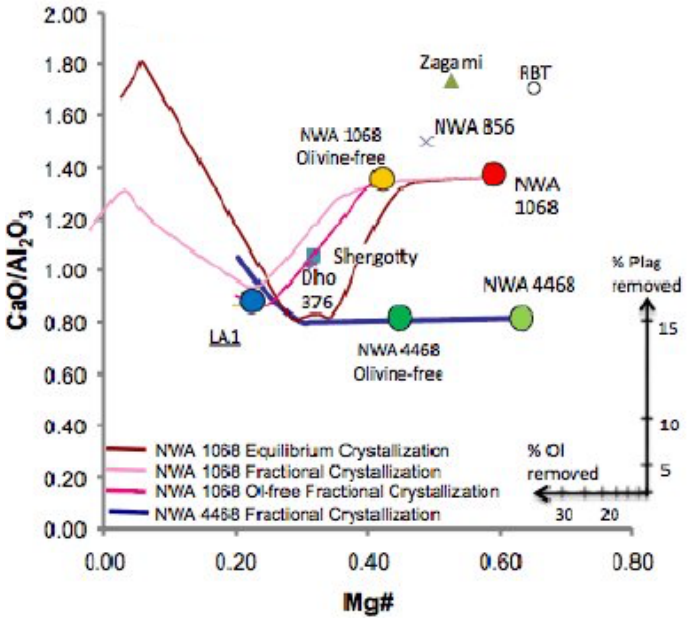

Figure 1. Crystallization paths modeled by the MELTS calculations done by Marks et al. (2010), shows the compositional evolution of liquids during crystallization. Olivine-free compositions account for accumulation and are calculated by subtracting 30% Fo_{71}olivine. (Marks et al., 2010.)

Chapter 3: Methodology

3.1 Introduction

NWA 4468 was studied using a multi-analytical approach that involved petrographic observations including the use of back-scattered electron images and x-ray element maps which helped characterize the samples, followed by targeted Electron Microprobe analysis for major elements and Laser Ablation Inductively Coupled Plasma Mass Spectrometry (LA-ICP-MS) analysis for trace and ultra-trace elements. The quantitative data collected using these techniques was used for thermometry and bathometry calculations, and to detect minor elements.

3.2 Preparation

Four pieces (~1mm diameter) of the basaltic shergottite NWA 4468 were purchased from the 675g original meteorite. The grains were mounted in a 2.54 cm diameter brass disc. 1 part hardener to 4 parts epoxy was used to form a disc that was removed from the brass casing after hardening. The disc containing all four grains was then sanded down using a fine grit to expose the grain surfaces. 1µm alumina followed by 0.3 µm alumina was the used to fine polish the samples.

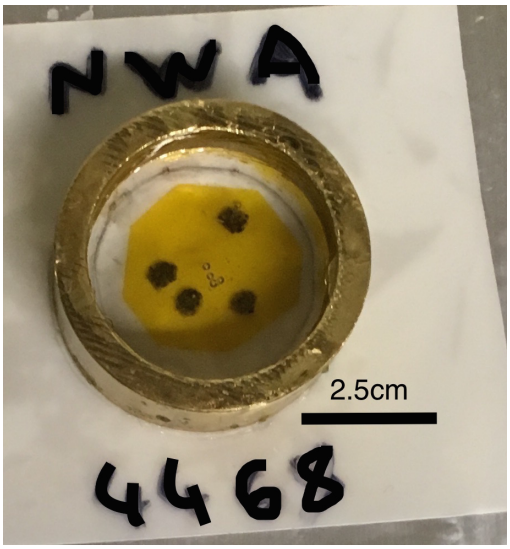

Figure 2. Grains of NWA 4468 while epoxy was hardening in the brass ring container.

3.3 Petrology

Each meteorite grain was observed under a polarizing light Nikon ECLIPSE 50iPOL microscope to determine the general number and size of the individual mineral crystals present in each meteorite grain. The A digital camera was setup to the microscope and photos were taken of the grains. The size of the grains was greater than the 2.5 mm field of view of the microscope. Between three and eight overlapping photos (depending on grain size) were taken of each grain, the photos were stitched together using PTGui Pro software. Control points on each photo were determined by petrographic and specific pixels.

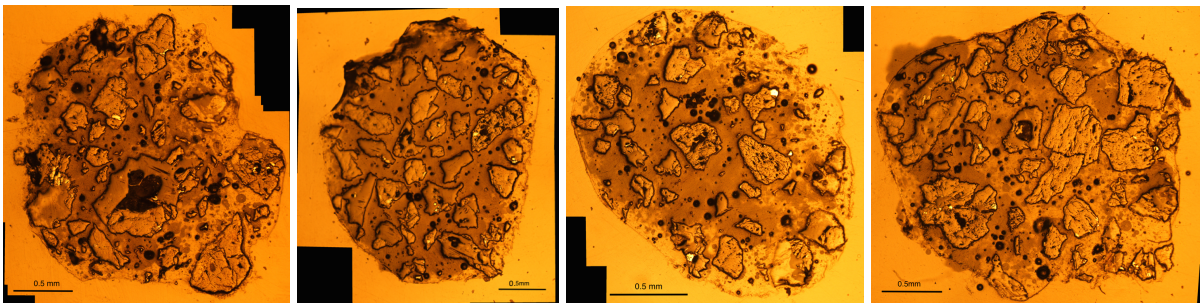

Figure 3. NWA 4468 photographed grains under polarized reflected light.

3.4 Electron microprobe

3.4.1 Operation of electron microprobe

The JEOL JXA-8200 Electron Probe Micro-Analyzer (EPMA) is located in the Robert M. MacKay Electron Microprobe Laboratory at Dalhousie University. It was used to collect backscattering Electron Images (BSE), X-ray element maps and to subsequently acquire detailed point element analysis of areas within each individual mineral. X-ray element maps and point analysis was carried out using the five wavelength-dispersive x-ray spectrometers (WDS) to collect x-rays emitted from the sample. This produced x-rays of element maps and major and minor data point analysis. The wavelength-dispersive spectroscopy crystals used for this analysis were PETJ, LIF, LIFH, TAP, TAPH diffractor crystals. The beam current was set at 20.00 nA for all analyses and the accelerating voltage was 15 kV.

The microprobes WDS was first used to collect BSE images of each whole rock grain of NWA 4468. A BSE detector collect the electrons that have been scattered from the surface of the mineral and reflect the mean atomic number of the minerals present. This results in an image that are closer to white than that of elements with lower atomic numbers. The greyscale images represent the contrast in mineral composition and can be used to determine different minerals and textures present throughout the grains.

3.4.2 X-ray compositional mapping

X-ray compositional maps were produced by the scanning of the electron beam point across a given area. The outcome are X-ray map images that show the distribution of elements within a given area. The brightest colours depict where the element of interest is most abundant, and the darker shades indicate areas where the element is less abundant. X-ray compositional maps were done using a spot diameter of 3μm, except for the five maps made of olivine grains with P zoning that used a 2μm diameter. Dwell times for all maps was 50.00 ms. X-ray maps were taken for Ca, Mn, Na, Al, Fe, Cr, Ti, Mg, Si, Ni in pyroxene crystals. Initial olivine maps were taken for Ca, Mn, Mg, P, Fe, Cr, Ni, Al, Si, Co. Secondary maps at a higher resolution were made for the five olivine crystals where phosphorous zoning had been observed in initial maps, these maps more detailed maps were taken using Ca, Cr, Al, P and Ni as the elements of interest.

3.4.3 Point analyses

Linear profile analysis was performed on 27 olivine grains, 21 pyroxene grains and 8 oxides using acceleration voltages of 15 kV and a beam current of 10 nA. Concentrations of calcium (Ca), magnesium (Mg), iron (Fe), manganese (Mn) and silica (Si) collected for all analyzed olivine crystals. A second analysis of olivine crystals with phosphorous zoning analyzed the same elements as the previous analyses as well as chromium (Cr), aluminium (Al), phosphorous (P) and nickel (Ni). Point analysis on pyroxenes crystals measured concentration of potassium (K), Ca, titanium (Ti), Cr, sodium (Na), Mg, Al, Fe, Mn, and Si. Oxide analysis determined concentration of K, Ca, Ti, Na, Mg, Al, Fe, Mn, Si. 15-40 were taken across each pyroxene or olivine crystal (depended on the size of the crystal). Yana's notes

EMP analyzes were reported as weight present of oxides, which were used to calculate cations per fomula unit using molecular mass of the oxides, and then calculate end-member composition using the stoichiometry. (Data reduction tables retrieved from Brady and Perkins, 2017)

$$Molecular\ cation = \frac{\#\ cations * weight\ \%\ of\ oxide\ from\ microprob}{molecular\ wieght\ \%\ of\ single\ oxide}$$

$$Molecular\ oxygen = \frac{\#\ oxygens * wieght\ \%\ of\ oxide\ from\ microprob}{molecular\ wieght\ \%\ if\ single\ oxide}$$

$$Normalized\ Cation = \frac{ideal\ \#\ of\ atomic\ units\ of\ mineral * molecular\ cation\ of\ element}{Total\ number\ of\ molecular\ cations\ of\ mineral}$$

$$Normalized\ oxygen = \frac{normalized\ cation\ of\ element * \#\ of\ oxygen\ in\ oxid}{\#\ of\ cations\ for\ individula\ oxide}$$

$$End\ memeber = \frac{normalized\ cation\ of\ choosen\ element\ end\ memeber}{Total\ normalized\ cation\ of\ endmembers}$$

Ternary diagrams are a useful way of representing the mineralogical composition of within given crystal. Triplot is a trilinear plotting program software that allows for an data points to be plotted (Todd Thompson Software). Ternary plots were made for Enstatite-Ferrosilite-Wollastonite ratios throughout pyroxene crystals as well as the ratio of olivine end members Fayalite-Forsterite.

3.5 Laser Ablation

LA-ICP-MS was performed on five olivine crystals using the Dalhousie Laser Ablation (ICP-MS) Laboratory at the Health and Environments Research Center Laboratory (HERC). Olivines were analyzed using a single spot laser with a repetition rate of 10Hz and spot size of 30 micros. Each analyses spanned 140 seconds, with the first 20 seconds being used for background

calibration, followed by 60 seconds of ablation and a 60 second cell washout period using He. NIST 610 glass and BHV 86 was used as standard reference material and analysed every 5 to 15 points. Si^{29} $Li^{7}Na^{23}$ Al^{27} P^{31} K^{39} Ca^{42} $Sc^{45}Ti^{49}$ V^{51} Cr^{53} Si^{29} $Co^{59}Ni^{60}$ Cu^{65} Zn^{66} Rb^{85} $Sr^{86}Sr^{88}$ Y^{89} Zr^{90} Ba^{137} Ba^{138} and Ce^{140} isotopes were analyzed with the Iolite version 3.6 software package which reduce data using Silica data from calculated from the EPMA as the internal standard.

3.6 Geothermometry

3.6.1 Aluminum-in-olivine

The maximum crystallization temperatures of the olivine crystals was determined using a temperature-dependant Al exchange between Cr-spinel and olivine (Coogan et al. 2014) were originally determined by Wan et al. (2008) and further modified by Coogan et al. 2014 to be calibrated for a larger range of Cr# (spinel-chrome numbers). This equation is not significantly affected by H_2O content or fO_2 (Coogan et al. 2014). These temperatures were then compared with geothermobarometers determined using Al-in-olivine for garnet peridotites (De Hoog et al., 2010 and Busswiler et al., 2017) . Although, these thermobarometers are less reliable because data spinel data was used instead of garnet.

$$\mathrm{T}(°\mathrm{K}) = \frac{10000}{0.575(0.162)+0.884(0.043)Cr\#-0.897(0.025)\ln(k_d)}$$

$$k_d = \frac{{Al_2O_3}^{Olivine}}{{Al_2O_3}^{Spinel}}$$

$$Cr\# = \frac{Cr^{spinel}}{[Cr+Al]^{spinel}}$$

3.6.2 Two-pyroxene

Two-pyroxene thermobarometer using the metastable conditions of the miscibility gap determined the crystallization pressure and temperatures of pyroxene crystals, using Fe-Mg exchange partition to determine whether the grains are at equilibrium (Davie and Boyd, 1996). This was further modified for Martian meteorites taking into account the dependence of this

thermobarometer on Fe and the fact that Martian meteorites have much greater FeO and lower Al_2O_3 composition than most Terrestrial mafic rocks (Lessel and Putirka, 2015).

Terrestrial - calibration

$$\frac{10^4}{T(°C)} = 11.2 - 1.96\ln\left[\frac{X_{EnFs}^{Cpx}}{X_{EnFs}^{Opx}}\right] - 3.3\left[X_{Ca}^{Cpx}\right] - 25.8\left[X_{CrCaTs}^{Cpx}\right] + 33.4\left[X_{Mn}^{Opx}\right] - 23.6\left[X_{Na}^{Opx}\right] - 2.08\left[X_{En}^{Opx}\right] - 8.33\left[X_{Di}^{Cpx}\right] - 0.05P(kbar)$$

$$P(kbar) = -94.25 + 0.045T(℃) + 187.7\left[X_{Al(VI)}^{Opx}\right] + 246.8\left[X_{Fm_2Si_2O_6}^{Opx}\right] - 212.5\left[X_{En}^{Opx}\right] + 127.5\left[a_{En}^{Opx}\right] - \frac{1.66}{K_f} - 69.4\left[X_{EnFs}^{Cpx}\right] + 133.9\left[a_{Di}^{Cpx}\right]$$

Martian – calibration

$$\frac{1}{T(K)} = 6.664 \times 10^{-4} - 2.757 \times 10^{-5}[P(GPa)] + 1.499 \times 10^{-3}[Na^{Opx}] - 1.640 \times 10^{-4}[Fe^{2+Cpx}] + 6.664 \times 10^{-5}\left[X_{DiHd}^{Cpx}\right]^2 + 2.611 \times 10^{-4}[Fe(tot)^{opx}]^2 - 6.602 \times 10^{-8}\left[\frac{1}{X_{CaTs}^{Cpx}}\right] + 6.869 \times 10^{-8}\left[\frac{1}{Na^{opx}}\right] = 1.166 \times 10^{-8}\left[\frac{1}{X_{Fm_2Si_2O_6}^{Opx}}\right]$$

$$P(GPa) = -3.764 + 0.6739\left[X_{CaO}^{cpx}\right] + 33.45\left[X_{Jd}^{Cpx}\right] + 4.03\left[X_{DiHd}^{Cpx}\right] - 5.945\left[X_{Di}^{Opx}\right] + 3.320\left[\frac{X_{EnFs}^{Cpx}}{X_{Fm_2Si_2O_6}^{Opx}}\right] + 40.34\left[Al(tot)^{Cpx} * Al(tot)^{Opx}\right] - 75.80\left[(Al(tot)^{Cpx} * Na^{Cpx}) + (Al(tot)^{Opx} * Na^{Opx}\right.$$

$$K_D(Fe-Mg)^{Cpx-Opx} = 1.262 - 0.023\left[CaO\ (wt\%)\right]^{cpx}$$

Chapter 4: Result

4.1 Olivine

4.1.1 Micrographs

BSE images were taken of all the four NWA 4468 grains, about 35% of the minerals within the grains were Olivines. The 80 µm – 400 µm olivine crystals are euhedral to subhedral in shape with some grains having fractures. A few grains appear to be prismatic in form. Oxides are visible throughout the grains as inclusions, maskylonite (shock altered plagioclase) is also observed the grains.

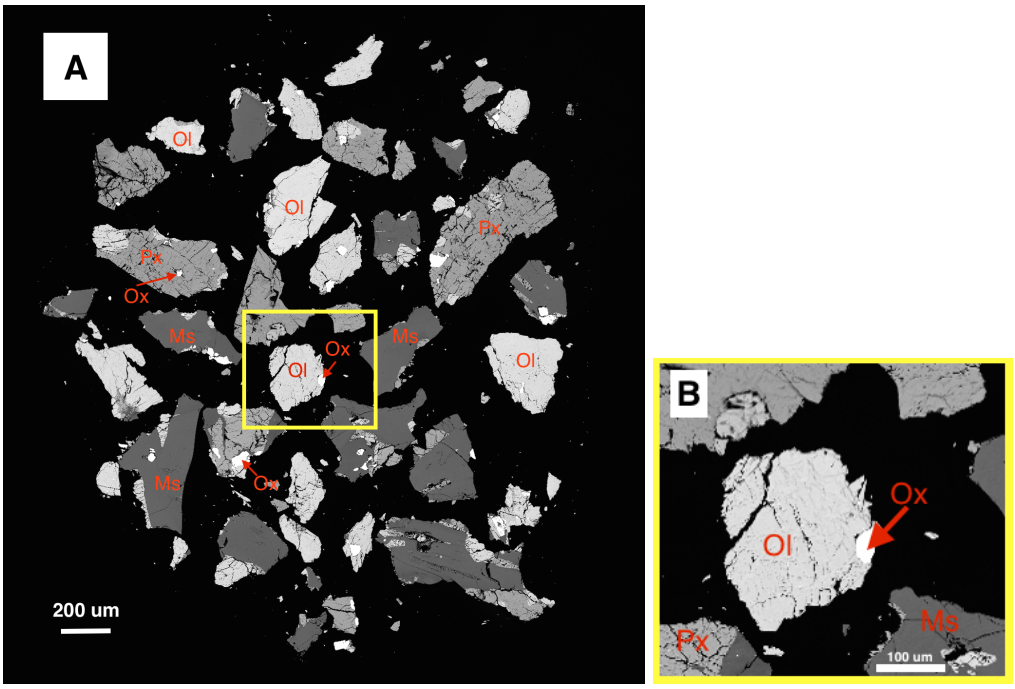

Figure 4. BSE image a grains from NWA 4468. (a) show the mineral distribution of olivine (Ol), pyroxenes (Px), maksylonite (Ms) and oxides (Ox) in a grass matrix. (b) Enlarged section shows lightly fractured, subhedral orthorhombic olivine crystals.

4.1.2 Element maps

Compositional element maps where taken of 27 olivine crystals (figure 5, figure 6), and 7 more detailed maps where made using long dwell time high resolution maps depicting Ca, Cr, Al, P and Ni concentrations of grains that phosphorous zoning (figure 7).

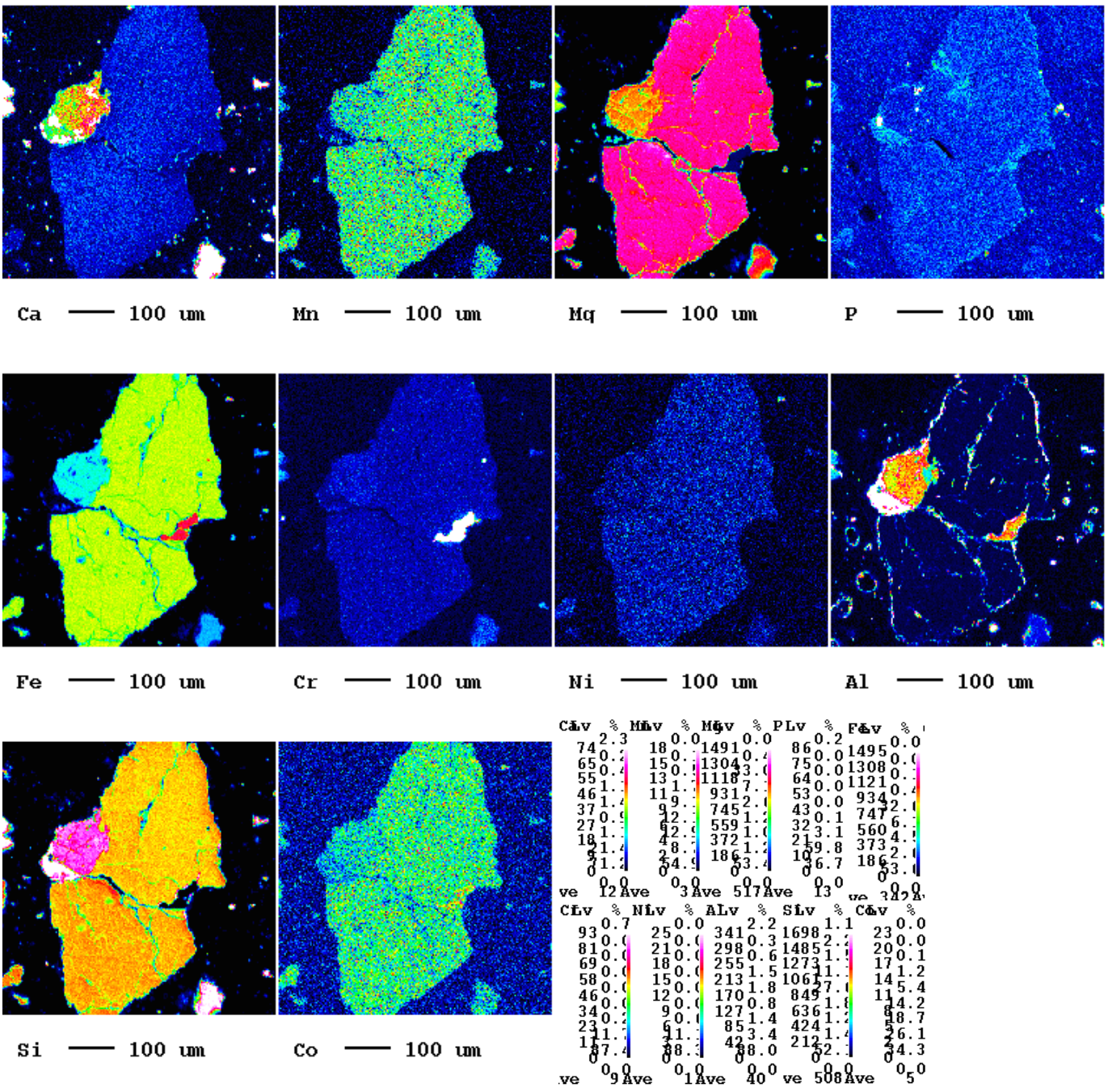

Figure 5. X-ray maps of olivine crystal. The colours depict the changing in concentrations of the elements in the crystal.

Most element maps of olivine crystals are homogenous in all elements analyzed except for Al, which appears along fractures within the crystal (figure 5.). This differs in about 20% of the grains which have phosphorous zoning with all other elements are homogenous (figure 6).

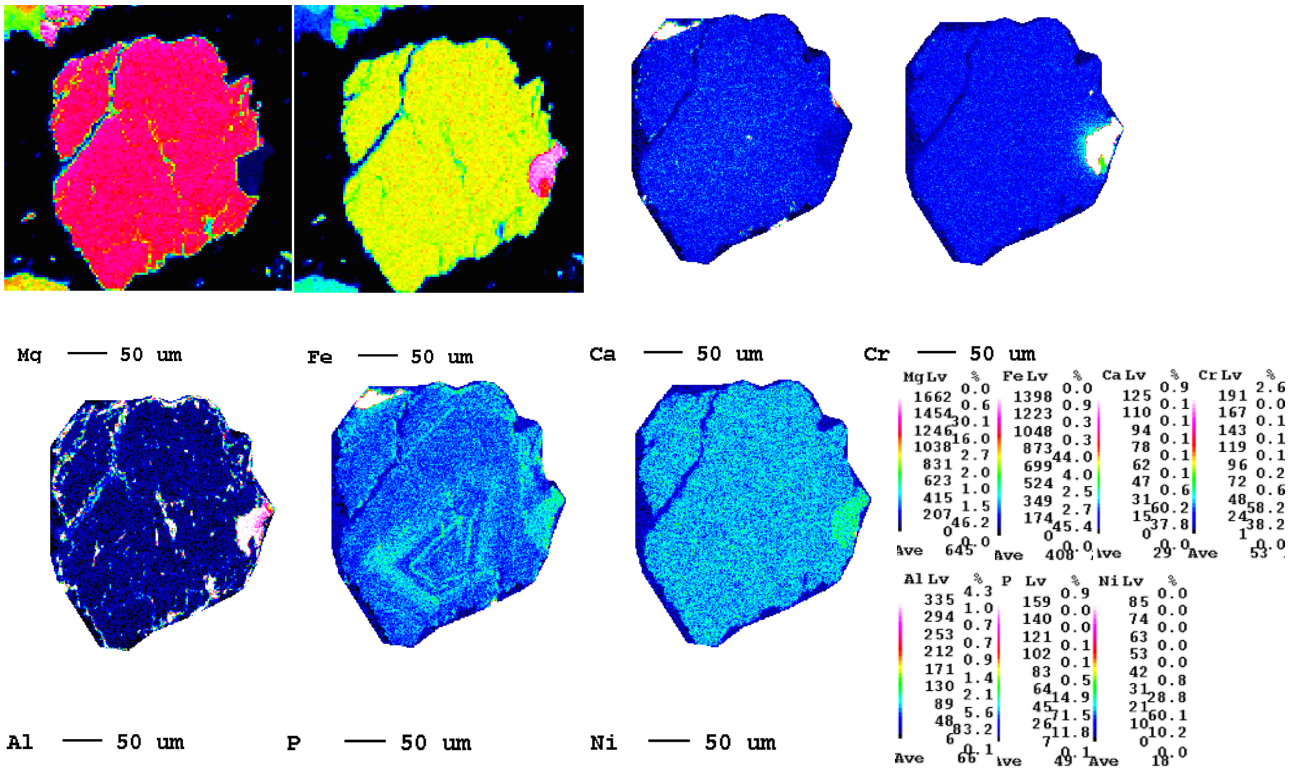

Figure 6. X-ray maps of olivine crystal. The colours depict the changing in concentrations of the elements in the crystal.

Five of the twenty-seven olivine crystals showed phosphorous zoning on the element concentrations maps, despite the homogeneity of Fe and Mg. Oscillatory and skeletal zoning patterns are seen in all the five grains. There are slight variations observed in zoning profiles with 3 of the grains showing an increase in phosphorous from core-to-rim (Fig 6. A, B, C,) where as one crystals has decreasing amount of in phosphorous towards the rim (Fig. 6, D) and one crystals has almost no oscillatory variation (Fig. 6, E).

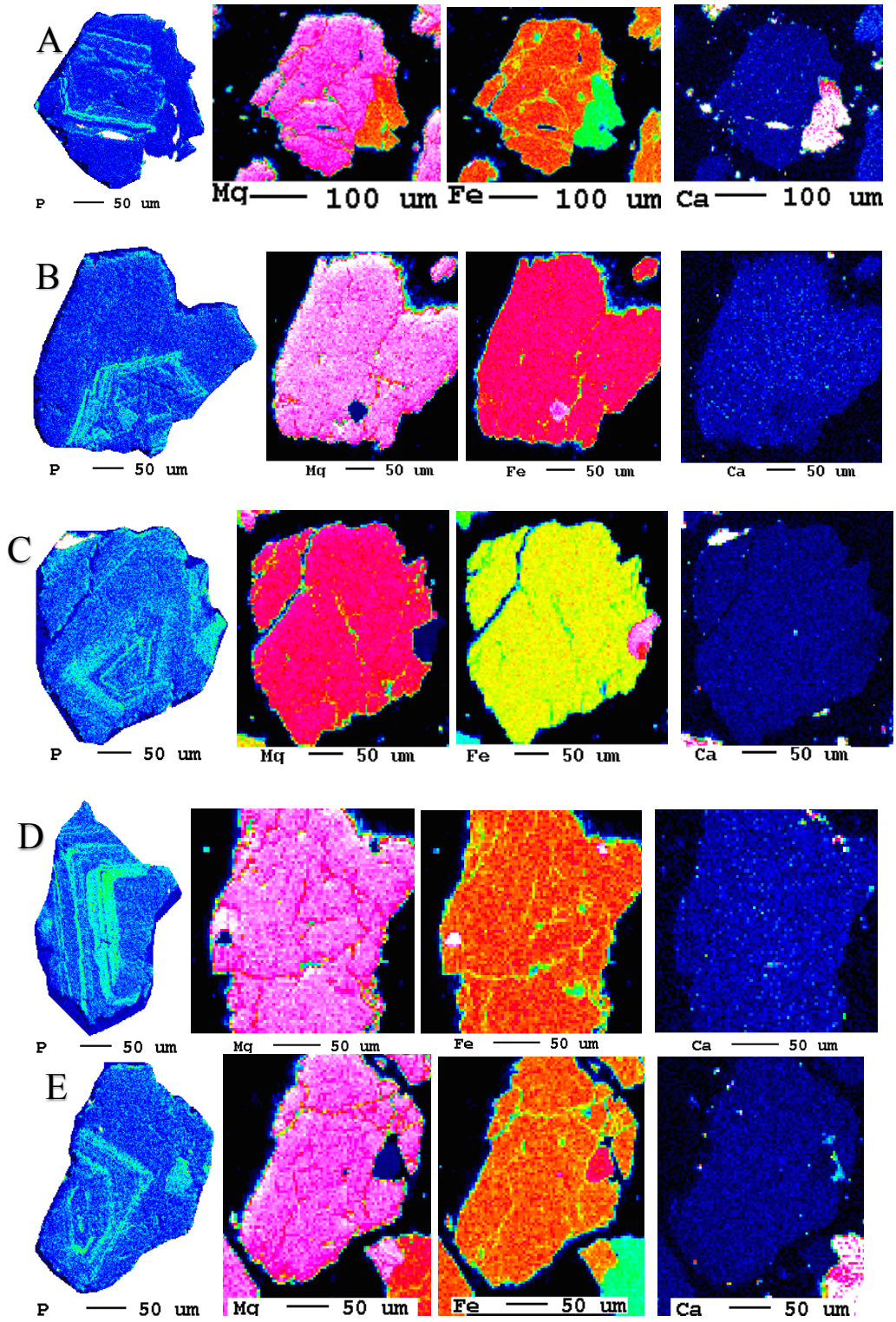

Figure 7. Detailed X-ray maps of the olivine crystals that showed phosphorous zoning. The colours depict the changing in concentrations of phosphorous throughout the crystal.

4.1.3 Line Scans

The microprobe's WD-spectrometer was used to collect points across a set linear traverses. Figure 8 and 9 displays the same 160µm traverse taken at 13 points with 15µm intervals. There appears to be little variation in the zoning profiles of the molecular percentage between olivine's end members (forsterite and fayalite). The molecular percentage of phosphorous was measured across the same traverse (Fig. 9). Although the molecular percentage of phosphorous is much less than that of Mg and Fe, greater changes can be seen across the traverse and changes can be observed within the area of the grain where phosphorous zoning takes places.

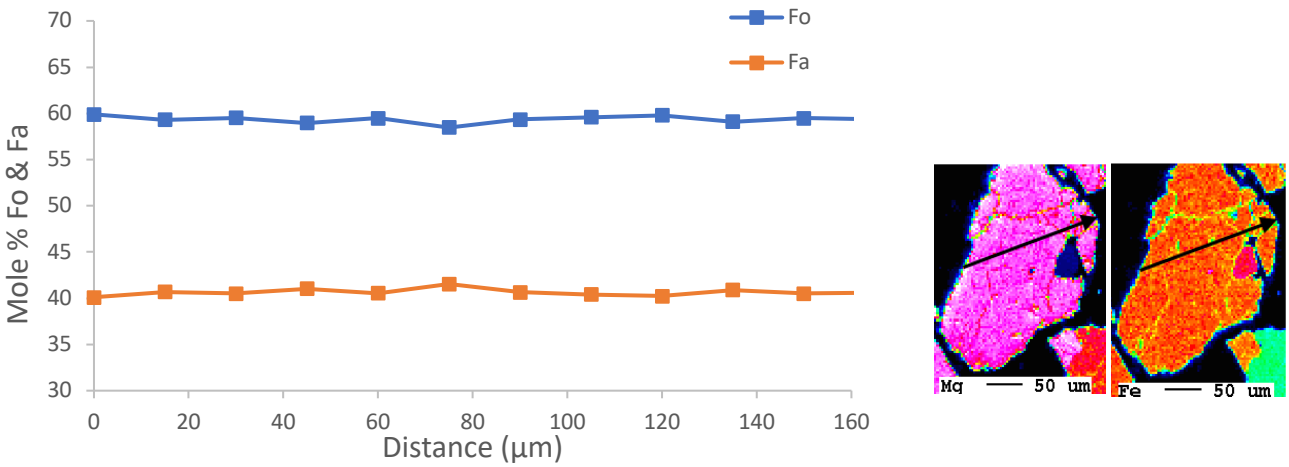

Figure 8. Molecular percent of forsterite compared to faylite along line scan of crystal olivine (13 point, 15 µm) and Mg and Fe element x-ray maps showing where the line scan was taken.

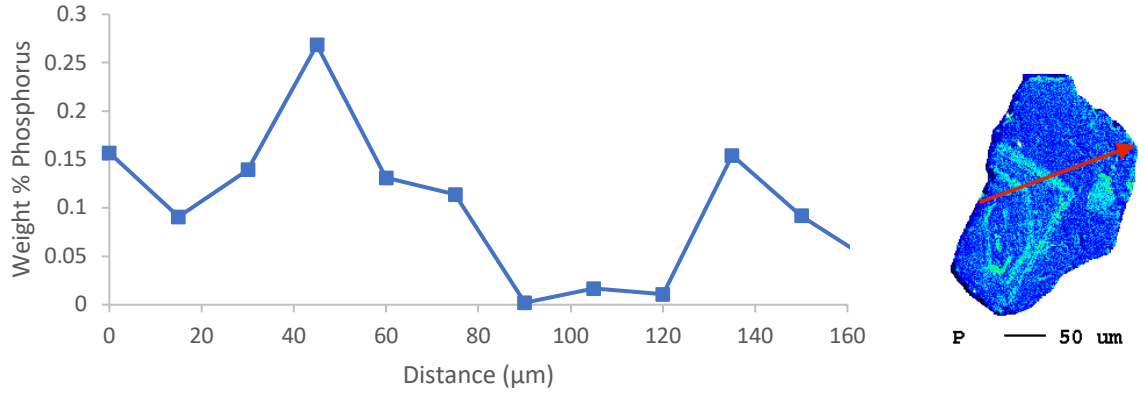

Figure 9. Phosphorus weight percentage along line scan (13 points, 15 µm) across olivine crystal showing changes in phosphorous weight percent and phosphorous element x-ray maps showing where the line scan was taken.

4.1.4 Compositional differences in P-zoned and P-unzoned crystals

The frequency of the forsterite molecular percentages in olivine crystals is shown in a histogram (Figure 9) and phosphorous zoned and non-zoned crystals show very similar percentages. The phosphorous zoned grains seem to have a larger range forsterite molecular percentage than the non-zoned grained.

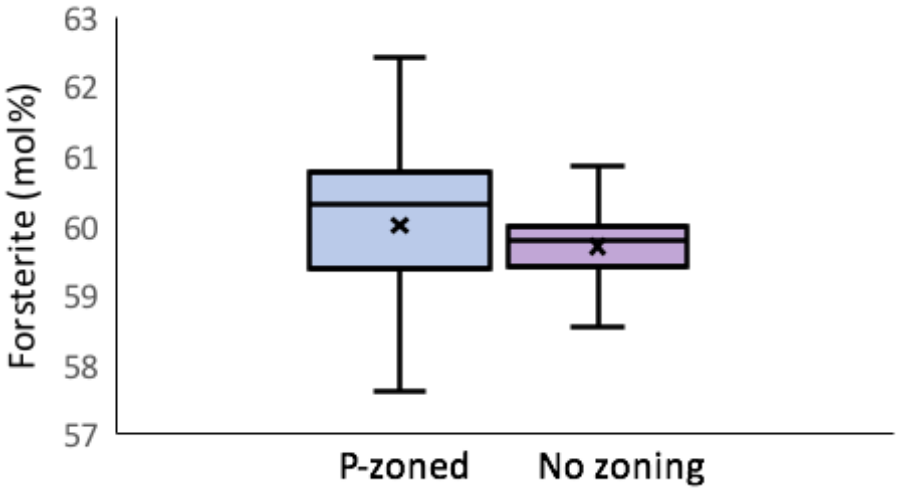

Figure 10. Forsterite molecular percentage in olivine crystals that have P-zoning compared to no p-zoning

4.1.5 Aluminum-in-olivine Thermometer

A aluminum-in-olivine thermometer (Coogan et al. 2015) for Cr-spinel and olivine was used to determined temperatures of crystallizations of the olivine crystals. This yielded a maximum temperature range of 1402°C to 1910°C. The garnet-olivine thermobarmeters by De Hoog et al. (2010) and Bussweller et al. (2017) (table 2) substituting spinel data for garnet, yielded a wider variation in temperatures as they are pressure dependent and calibrated for garnet. The values of the three thermometers were most similar at higher pressures. Falling within error of the aluminum-in-olivine thermometer around 40-80 kbar. These temperatures are likely slightly lower than the actual crystallization maximum as a result of using Si as an internal standard although the comparison of the between the EMP and LA-ICP-MS data are within in error of each.

Table 1. Temperatures and Pressures calculated using Aluminium- in-Olivine thermometry (Coogan et al. 2014)

	grain 3 olv1 (1)	grain 3 olv1 (2)	grain 3 olv1 (3)	grain 3 olv1 (4)	grain 3 olv1 (5)	grain 2 olv2 (1)	grain 2 olv2 (2)	grain 2 olv2 (3)	grain 2 olv2 (4)	grain 2 olv2 (5)	grain1 olv4 (1)	grain1 olv4 (2)	grain1 olv4 (3)	grain1 olv4 (4)
Coogan et al. 2014														
Al(ppm)	134.3	107.3	128	116.1	116.9	361	202.4	139	166.3	184.3	180.7	174	260	160.3
Cr# Spl min	0.8582	0.8582	0.8582	0.8582	0.8582	0.8527	0.8527	0.8527	0.8527	0.8527	0.8508	0.8508	0.8508	0.8508
Cr# Spl max	0.8518	0.8518	0.8518	0.8518	0.8518	0.8595	0.8595	0.8595	0.8595	0.8595	0.8684	0.8684	0.8684	0.8684
Al_2O_3 (ppm) Olv	0.025	0.020	0.024	0.022	0.022	0.068	0.038	0.026	0.031	0.035	0.034	0.033	0.049	0.030
Al_2O_3 (ppm)Spinel min	3.5674	3.5674	3.5674	3.5674	3.5674	4.2585	4.2585	4.2585	4.2585	4.2585	4.8175	4.8175	4.8175	4.8175
max	5.8463	5.8463	5.8463	5.8463	5.8463	5.0573	5.0573	5.0573	5.0573	5.0573	5.5564	5.5564	5.5564	5.5564
Kd min	0.0071	0.0057	0.0068	0.0061	0.0062	0.016	0.009	0.0062	0.0074	0.0082	0.0071	0.0068	0.0102	0.0063
Kd max	0.0043	0.0035	0.0041	0.0038	0.0038	0.0135	0.0076	0.0052	0.0062	0.0069	0.0061	0.0059	0.0088	0.0054
T (K) max	1733	1674.6	1720.2	1694.7	1696.4	1985.2	1799.7	1696.8	1744.4	1772.9	1734	1723.9	1838	1702.3
min	1610.9	1560.3	1599.8	1577.7	1579.2	1924	1749.3	1651.9	1697	1724	1691.9	1682.2	1790.8	1661.7
T (°C) max	1460	1402	1447	1422	1423	1712	1527	1424	1471	1500	1461	1451	1565	1429
T (°C) min	1338	1287	1327	1305	1306	1651	1476	1379	1424	1451	1419	1409	1518	1389
Average	1399	1344.4	1387	1363.2	1364.8	1681.6	1501.5	1401.4	1447.7	1475.4	1439.9	1430	1541.4	1409
Bussweiler et al. 2017														
Al (ppm) Olv	134.3	107.3	128	116.1	116.9	361	202.4	139	166.3	184.3	180.7	174	260	160.3
T (°C) 30 kb	1164.9	1129.1	1157.1	1141.5	1142.6	1347.4	1235.4	1170.6	1200.8	1218.7	1215.2	1208.6	1281.9	1194.5
T (°C) 40 kb	1217.3	1180.2	1209.2	1193	1194.1	1406.5	1290.4	1223.2	1254.5	1273.1	1269.5	1262.6	1338.6	1248
T (°C)50 kb	1269.7	1231.3	1261.3	1244.6	1245.7	1465.5	1345.3	1275.8	1308.2	1327.4	1323.7	1316.6	1395.2	1301.5
T (°C)60 kb	1322.1	1282.4	1313.4	1296.1	1297.3	1524.6	1400.3	1328.4	1361.9	1381.8	1377.9	1370.6	1451.9	1354.9
De Hoog et al (2010)														
Al (ppm) in Olivine	134.3	107.3	128	116.1	116.9	361	202.4	139	166.3	184.3	180.7	174	260	160.3
Cr (ppm)	77.6	91.7	103.3	99.4	97.4	83.2	38.7	47.1	58.9	71	57.4	198	214	76.6
Cr# Olv	0.3662	0.4608	0.4466	0.4613	0.4545	0.1873	0.1605	0.2531	0.2615	0.2781	0.2411	0.5323	0.4515	0.3233
T (°C) 15 kb	1005.1	992.39	1015.4	1004	1003.6	1128.9	1022.6	985.45	1014.5	1034.5	1022.9	1082.6	1132.9	1022.7
T (°C) 20 kb	1095.7	1080.7	1105.5	1093.1	1092.7	1231.4	1117.8	1076.4	1107.5	1128.6	1116.8	1176.1	1231.1	1115.2
T (°C)40 kb	1156.1	1139.5	1165.6	1152.5	1152.2	1299.8	1181.2	1137.1	1169.5	1191.3	1179.4	1238.4	1296.6	1176.9
T (°C)80 kb	1397.7	1374.9	1405.8	1390	1389.9	1573.2	1435.1	1379.7	1417.3	1442.3	1429.8	1487.6	1558.6	1423.7

	grain1 olv1 (1)	grain1 olv1 (2)	grain1 olv1 (3)	grain1 olv1 (4)	grain1 olv1 (5)	grain1 olv1 (6)	grain4 olv BR (1)	grain4 olv BR (2)	grain4 olv BR (3)	grain4 olv BR (4)	grain4 olv BR (5)	grain4 olv1 TL (1)	grain4 olv1 TL (2)	grain4 olv1 TL (4)	grain4 olv1 TL (5)	
Coogan et al. 2014																
Al(ppm)	207.6	213.7	270	188.4	175.5	301	366	179.6	176.1	130.1	290	277	570	157.7	122.1	
Cr# Spl min	0.8508	0.8508	0.8508	0.8508	0.8508	0.8508	0.8519	0.8519	0.8519	0.8519	0.8519	0.8519	0.8519	0.8519	0.8519	
max	0.8684	0.8684	0.8684	0.8684	0.8684	0.8684	0.8544	0.8544	0.8544	0.8544	0.8544	0.8544	0.8544	0.8544	0.8544	
Al2O3 Olv	0.039	0.040	0.051	0.036	0.033	0.057	0.069	0.034	0.033	0.025	0.055	0.052	0.108	0.030	0.023	
Al2O3 Spinel min	4.8175	4.8175	4.8175	4.8175	4.8175	4.8175	4.0449	4.0449	4.0449	4.0449	4.0449	4.0449	4.0449	4.0449	4.0449	
max	5.5564	5.5564	5.5564	5.5564	5.5564	5.5564	4.1636	4.1636	4.1636	4.1636	4.1636	4.1636	4.1636	4.1636	4.1636	
Kd min	0.0081	0.0084	0.0106	0.0074	0.0069	0.0118	0.0171	0.0084	0.0082	0.0061	0.0135	0.0129	0.0266	0.0074	0.0057	
Kd max	0.0071	0.0073	0.0092	0.0064	0.006	0.0102	0.0166	0.0081	0.008	0.0059	0.0132	0.0126	0.0259	0.0072	0.0055	
T (K) max	1772.2	1780.4	1849.5	1745.3	1726.1	1883.5	2008.8	1780.4	1774.8	1693.2	1927.9	1912.8	2183.1	1744.2	1677.1	
min	1728.3	1736.1	1801.7	1702.7	1684.4	1833.9	1997.5	1771.5	1766	1685.2	1917.5	1902.5	2169.7	1735.6	1669.2	
T (°C) max	1499	1507	1577	1472	1453	1610	1736	1507	1502	1420	1655	1640	1910	1471	1404	
T (°C) min	1455	1463	1529	1430	1411	1561	1724	1499	1493	1412	1645	1630	1897	1463	1396	Ave T
Average	1477.3	1485.3	1552.6	1451	1432.3	1585.7	1730.1	1503	1497.4	1416.2	1649.7	1634.6		1466.9	1400.1	1477.2
Bussweiler et al. 2017																
Al(ppm)	207.6	213.7	270	188.4	175.5	301	366	179.6	176.1	130.1	290	277	570	157.7	122.1	Averages
T (°C) 30 kbar	1240	1245.3	1289.2	1222.6	1210.1	1310.5	1350.3	1214.2	1210.7	1159.8	1303.1	1294.2	1448.3	1191.7	1149.5	1227.2
T (°C) 40 kbar	1295.1	1300.6	1346.1	1277.1	1264.2	1368.2	1409.4	1268.4	1264.8	1212	1360.6	1351.3	1511.1	1245.1	1201.3	1281.9
T (°C)50 kbar	1350.2	1355.9	1403	1331.6	1318.2	1425.9	1468.6	1322.5	1318.9	1264.2	1418	1408.4	1573.8	1298.5	1253.2	1336.5
T (°C)60 kbar	1405.4	1411.2	1460	1386.1	1372.3	1483.6	1527.7	1376.7	1372.9	1316.4	1475.4	1465.5	1636.5	1351.8	1305	1391.2
De Hoog et al (2010)																
Al(ppm)	207.6	213.7	270	188.4	175.5	301	366	179.6	176.1	130.1	290	277	570	157.7	122.1	Averages
Cr(ppm)	135.8	138.2	300	145.9	121.7	277	1430	109.2	108.9	85.9	75.5	95	2730	263	139	1072.6
Cr# Olv	0.3955	0.3927	0.5263	0.4364	0.4095	0.4792	0.7962	0.3781	0.3821	0.3977	0.2066	0.2554	0.8273	0.6251	0.5324	1167.2
T (°C) 15 kbar	1080.8	1085	1157.5	1074	1056.3	1166.3	1282.3	1053	1050.7	1007.2	1093.8	1097.5	1388.1	1087.4	1026.9	1230.3
T (°C) 20 kbar	1176.3	1180.9	1256.2	1168.4	1149.9	1266.4	1385.1	1146.8	1144.3	1097.5	1193.5	1196.5	1497.2	1179.7	1116.5	1482.8
T (°C)40 kbar	1239.9	1244.8	1322	1231.3	1212.3	1333.1	1453.5	1209.3	1206.7	1157.6	1259.9	1262.5	1570	1241.3	1176.2	
T (°C)80 kbar	1494.6	1500.3	1585.2	1482.9	1461.7	1600.1	1727.4	1459.5	1456.3	1398.4	1525.6	1526.6	1861.1	1487.6	1415.2	

4.2 Pyroxene

4.2.1 Micrographs

NWA 4468 is about 30% pyroxene grains (Fig 12-A). The pyroxene grains are euhedral to subhedral in shape. Most grains show cleavage and fractures with some grains also exhibiting exolution textures (Fig. 12-B). Grains general prismatic habit and range from 100 µm - 800 µm.

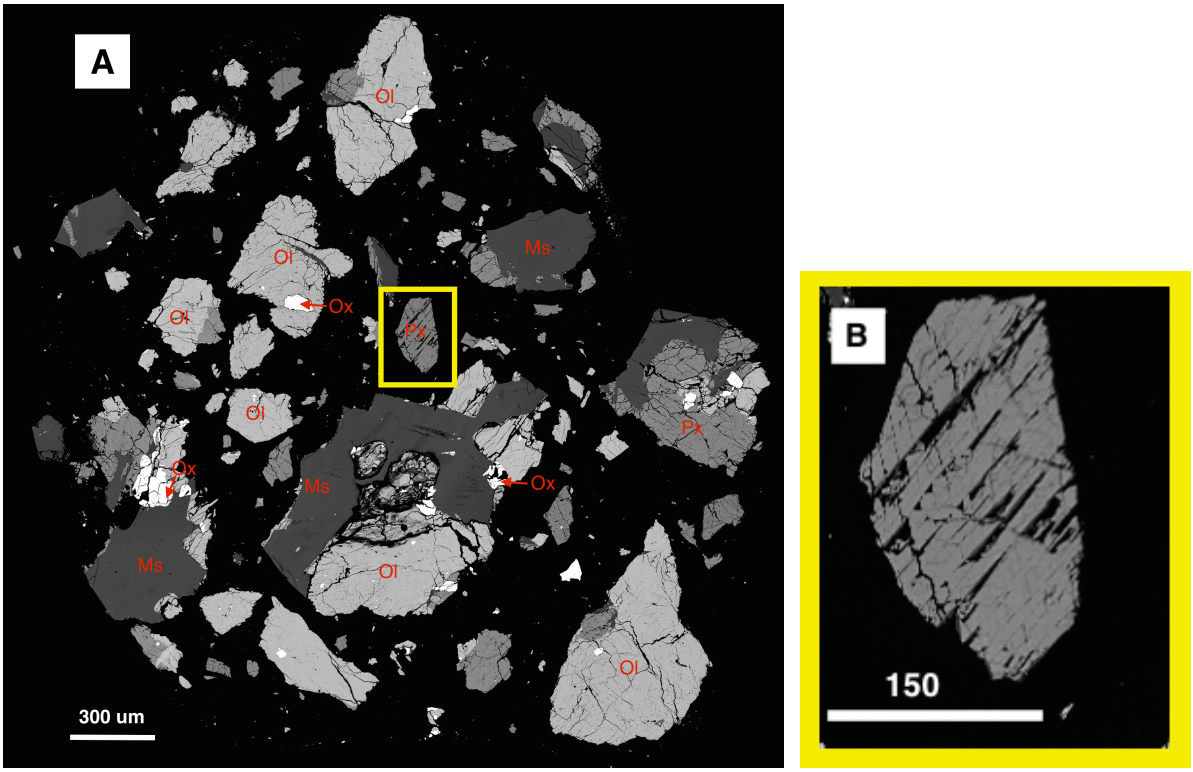

Figure 11. BSE image of a NWA 4468. (a) show the mineral distribution of olivine (Ol), pyroxenes (Px), maksylonite (Ms) and oxides (Ox) in a grass matrix. (b) Enlarged section shows cleavages and fractures run through pyroxene grain.

4.2.2 Element maps

Element x-ray maps show changes in compositions throughout the grains. The pyroxene grain shown in figure 11 exhibits oscillatory zoning as the concentrations vary between Mg and Fe rich zones. Ca and Na show an increase in the same zones as Mg, whereas Al seems to increase slightly in concentration in Fe rich zones and is present along fractures. Si is homogenous throughout the grain.

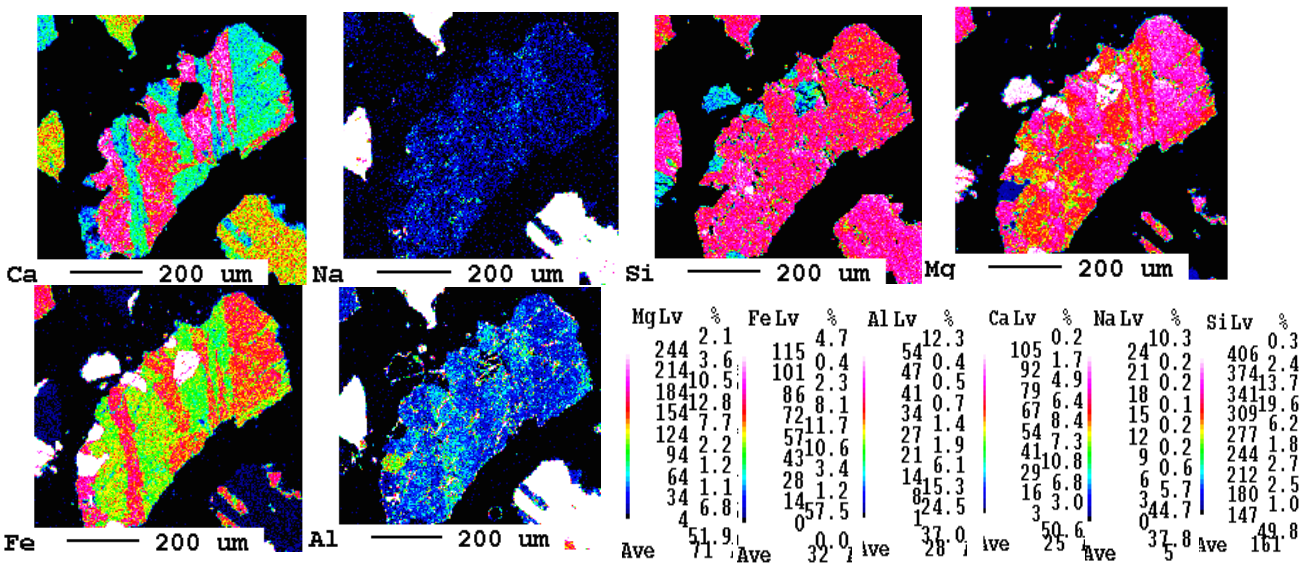

Figure 12. X-ray maps of Pyroxene crystal. The colours depict the changing concentrations of the elements within the crystal.

Some pyroxene crystal have minimal compositional variations (figure 12). Changes appear to be restricted to narrow, similarly oriented parallel zones that are likely exsolution lamellae.

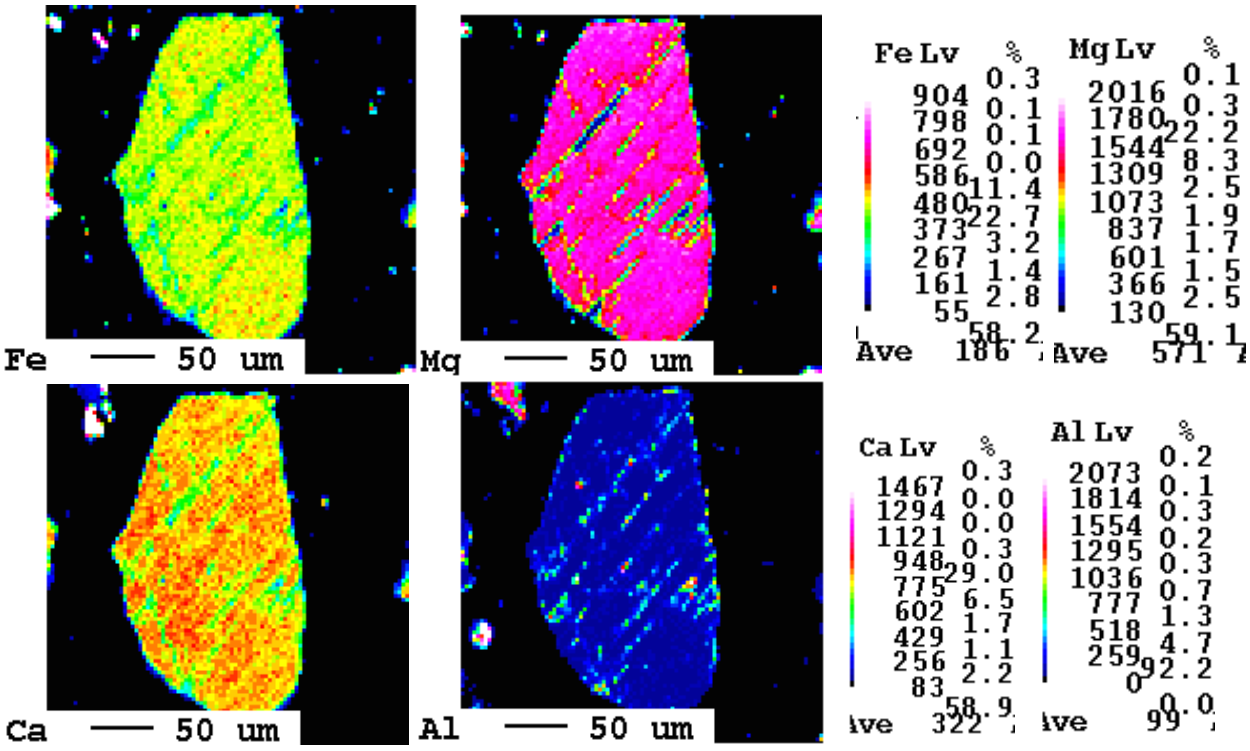

Figure 13. X-ray maps of Pyroxene crystal. The colours depict the changing concentrations of the elements within the crystal.

4.2.3 Line Scans

Figure 15. Show variations in molecular percent of Enstatite-Ferrosilite across 680 µm scan line of a pyroxene grain. The grain ranges from 65 % enstatite (35% ferrosilite) to 75% enstatite (25% ferrosilite). This scan traverse crosses four enstatite rich zones.

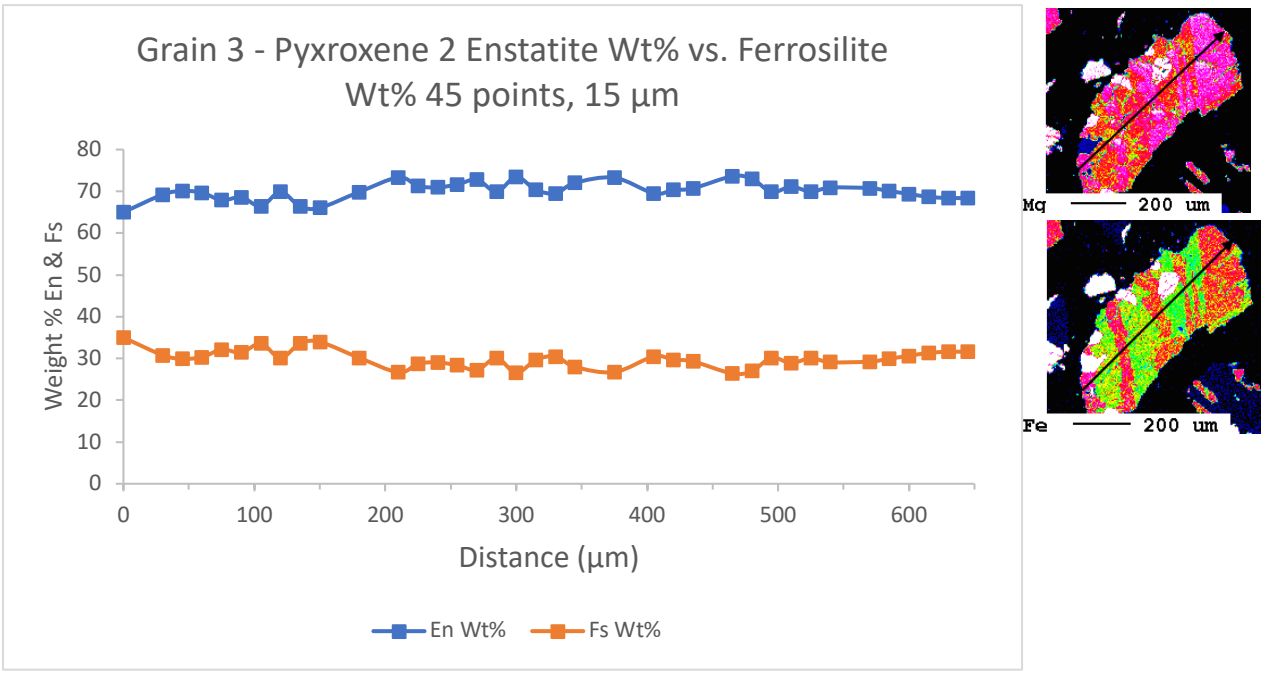

Figure 14. Molecular percentage of enstatie and ferrosilite along line scan (25 points, 15 µm) across pyroxene crystal depicting the changes in Forsterite weight percentages with respect of Fayalite weight percent and Fe, Mg element maps showing where the line scan was taken.

4.2.4 Triplot

The normalized data from the electron microprobe was plotted for Wo, En and Fs on a ternary diagram (Fig. 16). The data plots in two distinct zones, Augite and Pigeonite. All data point are confined to these to compositions with no points falling below 5% Ca or above 45% Ca.

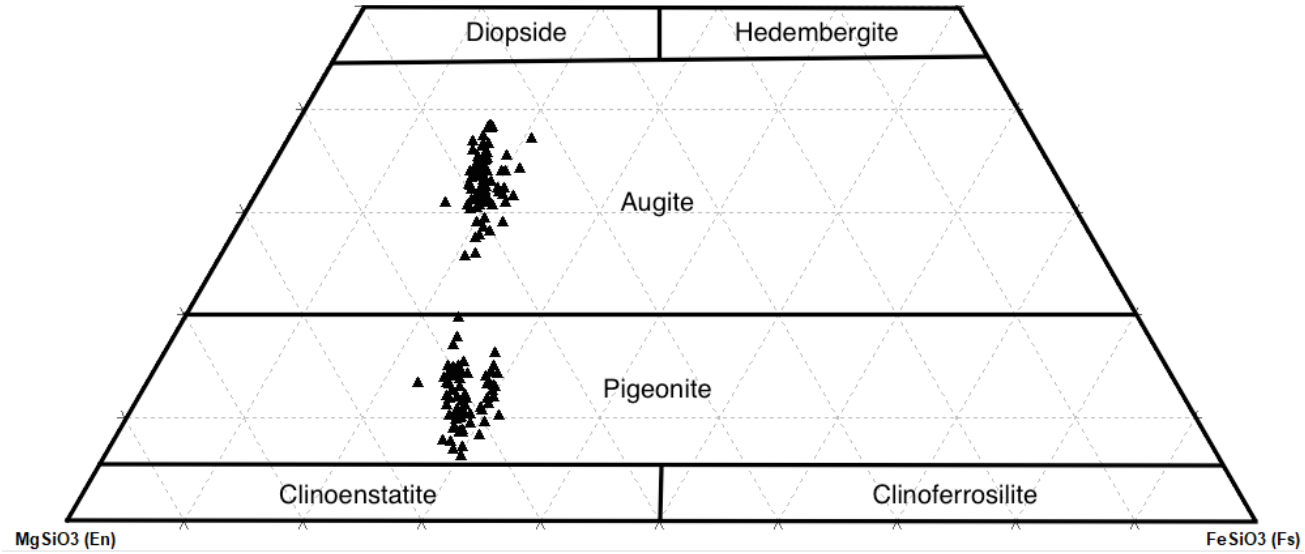

Figure 15. Ternary diagram of NWA 4468 pyroxene compositions.

4.2.5 Two-Pyroxene Thermobarometry

NWA 4468 has clear Ca rich and Ca-poor zones within the pyroxenes. The element data collected by the microprobe for the pyroxenes was used to calculate the temperature and pressures using average weight percentages of elements within the Ca-rich and Ca-poor zones of each mineral grain as well as the combined average of all the grains. Temperatures and pressures were also calculated using data throughout the crystals including the boundaries of Ca-rich and Ca-poor zones, the core of the zones, core vs. rims of both Ca-rich and Ca-poor variations and opposite rims of zones. Table 1 shows the results of these thermometer and barometer calculations using geothermobarometery determined by Lessel and Putirka (2015) which were calibrated for Martian igneous rock and Putrika (2008) calibrated for Terrestrial mafic rocks. Equilibrium for the Martian calibration is 0.942 ± 0.14 and 1.09 ± 0.14 for Terrestrial samples. Temperatures were range from 1092 °C to 1196 °C for pressures from 0 to 5 kbar for Martian calibrations. Whereas temperatures from 1104 °C to 1301°C were calculated from pressure ranging from 0 to 5 kbar using Terrestrial calibrations.

Table 2. Two-pyroxene thermometers calculated for temperatures between 0 and 5 Kbar, equations from Lessel and Putirka (2015) and Putirka (2008)

	Total average	Average grain 1, Pyroxene 1	Average, grain 2 pyroxene 1	Boundary, grain 2 pyroxene 1	Average, grain 2 pyroxene 1	Rim (clino) to Core (ortho), grain 2 pyroxene 1	Average, grain 3 pyroxene 1	Core to core, grain 3 pyroxene 1	Core (clino) to opposite rim (ortho), grain 3 pyroxene 1	Boundary, grain 3 pyroxene 1
Clinopyroxene Composition (Wt%)										
SiO_2	51.940	51.911	52.080	51.130	51.801	52.192	52.212	52.386	52.386	52.673
TiO_2	0.345	0.289	0.378	0.544	0.367	0.312	0.305	0.287	0.287	0.279
Al_2O_3	1.679	1.568	1.598	1.567	2.091	1.653	1.455	1.407	1.407	1.367
FeOt	11.249	10.696	11.977	12.991	10.587	11.591	11.036	11.666	11.666	10.601
MnO	0.439	0.420	0.487	0.545	0.397	0.436	0.421	0.462	0.462	0.419
MgO	16.396	16.034	16.520	15.411	15.881	16.555	16.584	16.869	16.869	16.543
CaO	15.611	16.171	14.933	14.498	16.656	15.222	15.932	14.732	14.732	16.513
N_2O	0.227	0.200	0.233	0.248	0.237	0.249	0.223	0.181	0.181	0.225
K_2O	0.031	0.026	0.039	0.077	0.027	0.023	0.028	0.018	0.018	0.025
Cr_2O_3	0.718	0.780	0.662	0.568	0.818	0.683	0.674	0.638	0.638	0.642
Orthopyroxene Composition (Wt %)										
SiO_2	52.661	51.831	53.457	52.878	53.101	53.677	52.994	53.677	52.193	53.046
TiO_2	0.223	0.356	0.274	0.181	0.201	0.181	0.171	0.181	0.202	0.222
Al_2O_3	1.047	1.035	0.837	0.605	1.144	1.186	0.947	1.186	1.045	1.330
FeOt	16.976	17.689	18.703	19.066	17.454	15.821	16.260	15.821	16.113	15.232
MnO	0.607	0.624	0.638	0.638	0.613	0.577	0.582	0.577	0.601	0.563
MgO	20.963	19.662	20.949	21.313	21.488	21.441	21.528	21.441	20.454	20.895
CaO	5.666	6.541	4.772	3.999	4.697	6.493	6.090	6.493	6.781	8.425
N_2O	0.091	0.124	0.089	0.052	0.082	0.094	0.092	0.094	0.097	0.146
K_2O	0.035	0.026	0.033	0.023	0.024	0.027	0.031	0.027	0.035	0.082
Cr_2O_3	0.399	0.406	0.305	0.240	0.411	0.515	0.431	0.515	0.409	0.534
Martian Calibration										
T(°C)	1153.38	1092.30	1126.91	1097.56	1117.85	1164.30	1138.98	1157.69	1125.17	1133.46
KD (Fe-Mg)	1.002	0.955	0.982	0.959	0.975	1.011	0.991	1.006	0.981	0.987
KD (Fe-Mg) T-independent	0.903	0.890	0.919	0.929	0.879	0.912	0.896	0.923	0.923	0.882
Terresterial Calibration										
T(°C)	1198.28	1205.08	1162.89	1129.30	1156.72	1249.09	1219.23	1252.64	1248.00	1327.32
KD(Fe-Mg)	0.847	0.741	0.812	0.942	0.821	0.949	0.881	0.937	0.878	0.879
Kf	0.614	0.770	0.476	0.397	0.568	0.660	0.676	0.629	0.674	0.978

	Average grain 3, pyroxene 2	Boundary 1, grain 3, pyroxene 2	Boundary 2, grain 3 pyroxene 2	Core to core, grain 3 pyroxene 2	Opposite edges, grain 3 pyroxene 2	Average, grain 4 pyroxene 1	Boundary grain 4 pyroxene 1	Core to core, grain 4 pyroxene 1
Clinopyroxene Composition (Wt%)								
SiO_2	51.668	52.212	52.692	51.681	51.407	51.970	52.169	51.822
TiO_2	0.376	0.228	0.289	0.301	0.643	0.255	0.257	0.252
Al_2O_3	1.583	1.507	1.566	1.573	1.557	1.397	1.350	1.352
FeOt	11.848	11.540	11.134	12.250	11.915	11.215	11.436	11.607
MnO	0.468	0.443	0.424	0.512	0.446	0.457	0.481	0.475
MgO	16.815	17.311	16.887	17.378	15.368	16.685	16.853	16.729
CaO	14.461	14.343	14.539	13.713	15.714	15.141	14.935	14.665
N_2O	0.224	0.201	0.172	0.190	0.321	0.224	0.241	0.190
K_2O	0.032	0.029	0.038	0.020	0.027	0.028	0.036	0.026
Cr_2O_3	0.701	0.706	0.826	0.667	0.598	0.619	0.579	0.627
Orthopyroxene Composition (Wt %)								
SiO_2	52.573	52.624	51.061	52.607	52.731	52.562	52.419	52.896
TiO2	0.240	0.219	0.190	0.231	0.221	0.162	0.154	0.177
Al_2O_3	1.279	1.154	2.787	1.116	1.229	0.920	1.003	0.868
FeOt	16.032	15.819	13.962	16.397	16.946	17.465	17.660	18.462
MnO	0.592	0.598	0.512	0.583	0.578	0.621	0.624	0.668
MgO	20.660	20.646	19.260	21.525	20.570	21.458	21.224	21.909
CaO	6.461	6.641	9.265	5.719	5.264	4.579	4.169	3.428
N_2O	0.088	0.099	0.109	0.113	0.091	0.082	0.072	0.061
K_2O	0.043	0.018	0.042	0.043	0.021	0.035	0.049	0.026
Cr_2O_3	0.473	0.502	0.569	0.493	0.437	0.327	0.339	0.289
Martian Calibration								
T(°C)	1168.00	1161.33	1168.45	1159.72	1196.35	1138.11	1135.77	1120.56
KD (Fe-Mg)	1.014	1.008	1.014	1.007	1.035	0.991	0.977	0.977
KD (Fe-Mg) T-independent	0.929	0.932	0.928	0.947	0.901	0.914	0.918	0.925
Terrestrial Calibration								
T(°C)	985.06	990.696	1024.12	1007.48	948.43	961.27	963.69	961.385
KD(Fe-Mg)	0.908	0.870	0.909	0.925	0.941	0.826	0.816	0.823
Kf	0.627	0.632	0.900	0.51	0.590	0.478	0.426	0.340

4.3 Bivariate Plots Comparing Olivine to Pyroxene

Olivine crystals have lower Mg# and CaO weight percentages than pyroxene crystals and higher MnO weight percentages (figure 17). This suggests that MnO was more readily available in the melt when olivines where crystallizing and CaO was taken up more in the crystallization of pyroxenes.

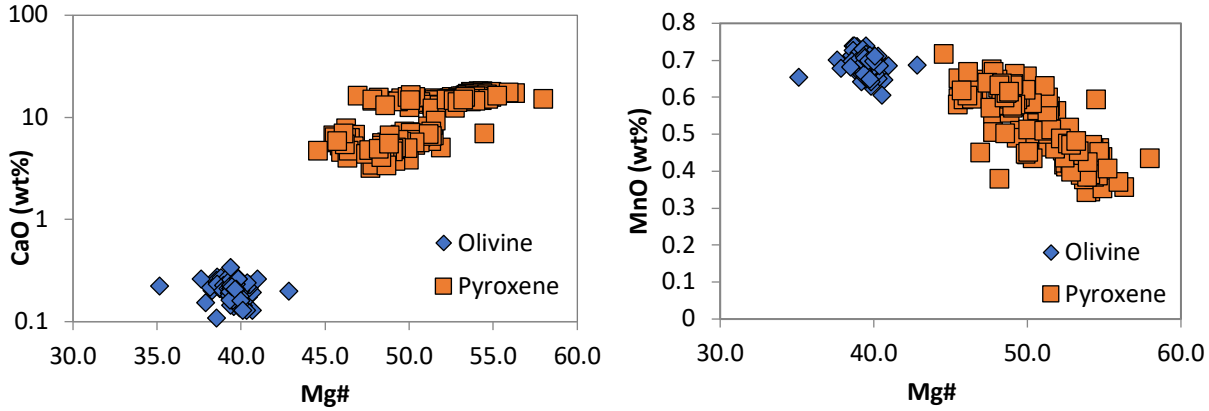

Figure 16.a) Pyroxene and Olivine Mg# vs. CaO (wt%) showing pyroxene having an increased Mg# and CaO wt%. b) Pyroxene and Olivine Mg# vs. MnO showing a decrease in MnO with increasing Mg.

Crystallization temperatures is higher for olivines then pyroxenes , with pyroxene having a larger distribution of temperatures and crystallization at higher temperatures (figure 18).

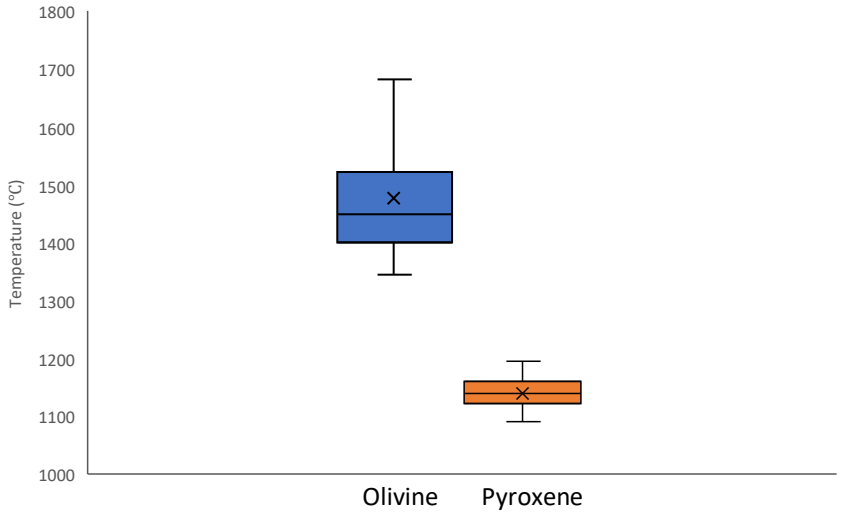

Figure 17. Distribution of temperatures observed in olivines and pyroxenes.

Chapter 5: Discussion

5.1 Crystallization History

Olivines are present in high abundance within NWA 4468. This mineral forms at high pressures and temperatures early on within a magma's cooling history. The bulk composition of Olivine is mostly iron and magnesium making it compositionally simple, meaning it can be used to determine the general minimum crystallization temperature. All the olivine crystals observed in this study have a homogenous iron and magnesium element profiles. Distinct P zoning occurs in about 20% of the olivine crystals. The presence of P in olivine crystals is typically the result of P^{5+} substituting for Si^{4+} in the olivine crystal structure (Agrell et al. 1998), although it can also be incorporated into the olivine tetrahedron coupled substitution of P with other prevalent elements (Al and Cr) (Milman-Barris et al., 2008). Since in this study the zoning of Al and Cr was not observed it can be assumed that P has substituted for Si. The oscillatory zoning observed in this study suggests the olivine crystals were growing at disequilibrium. These features reflect changes in internal factors of the crystal structure, that may or may not be influenced by external factors such as magma mixing events and eruptions (Milman-Barris et al., 2008). The skeletal shape of this zoning suggests that growth was diffusion controlled during rapid cooling (Faure et al., 2003). P zoning is preserved due to its diffusivity coefficient being two to four magnitudes of order lower than that of Fe and Mg (Chakraborty, 2010; Watson et al., 2015). The variation in zoned and unzoned P suggests that there may have been multiple crystallization stages of olivines, there is little variation seen in P and Ni chemical compositions between zoned and unzoned P. Furthermore, all the olivines that were observed to have phosphorous zoning had chromite inclusions, whereas only some of the non-phosphorous zoned olivines had inclusions.

There is distinctive compositional changes between Ca-rich and Ca-poor zones within most pyroxene crystals. It is impossible to determine crystal system of the minerals without the being able to observe the sample in thin section, which was not within this study due to the small sample size. Therefor it cannot be determine if the Ca-poor zones are orthopyroxene or augite. The distinct difference in compositions (Fig. 16) shows that the reaction was likely not continuous. The variation in Ca suggests crystallization of pyroxene grains occurred at multiple

temperatures with Ca-poor grains forming below the immiscibility gap (Aoki, 1964) and Ca-rich pyroxene crystalizing above it. Slow cooling rates resulted in exsolution lamellae are present within some crystals which is the result of solid state diffusion.

Two-pyroxene geothermobarometery calibrated for Martian meteorites (Lessel and Putrika, 2015) yielded temperatures to range from 1092°C to 1196 °C for pressures from 0 to 5 kbar. The temperature dependent (K_D) was determined to range between 0.973 and 1.014, at equilibrium temperature is predicted to be 0.942 ± 0.14. This suggests that the zones within most crystals are at equilibrium and therefore the equation is valid. Alternatively, the two-pyroxene geothermbarometery using terrestrial calibrations results in higher temperature values of 932.7°C to 1024.1°C over the same pressure range. The K_D values of the terrestrial calibration are from 0.741 to 0.949 which are below the K_D value for equilibrium (1.09 ± 0.14), suggesting that under terrestrial conditions with similar element percentages to igneous earth rocks, these samples are not at equilibrium. Therefore the temperatures and pressures calculated using the Martian calibration is likely to be more indicative of the crystallization of these grains.

Olivines have a higher crystallization temperatures then the pyroxenes suggest that (Fig. 18). There is no overlap in crystallization temperatures and olivine has a bell curve distribution with a slight tail at higher temperatures. The different crystallization temperatures, as well as the pyroxene oikocryst of the rock, with olivine grains being found within pyroxene oikocrysts suggests that the pyroxene and olivines did not crystallize at the same time.

There has been much discussion on the petrogenesis of Martian olivine phyric shergotties, and as to whether they are the product of magma mixing (Boctor et al., 1998; Mittlefehldt et al., 1999; Barrat et al., 2002) or the result of re-entrainment resulting in olivine cumulates (Usui et al., 2008). The higher magnesium number of pyroxene suggests that pyroxenes and olivines (figure 17) did not crystallize from the same melt. This study determined the olivine crystals in the NWA 4468 to compositionally range from has an olivine Fo_{61} - Fo_{58}, this is compositionally similar to the groundmass of LAR 06319 which ranges from Fo_{62} - Fo_{46} (Sarbadhikari, et al. 2009) and NWA 1068 which range from Fo_{42} to Fo_{75} (Herd, 2006; Shearer et al., 2008). These values are significantly lower than Earth's mantle that is compositionally

closer to Fo_{90} (Musselwhite et al., 2006) as well as that of the Martian mantle has a primitive Fo_{76} (Collinet at al., 2015) to Fo_{89} for mantle source of depleted shergottites (Musselwhite et al., 2006). NWA 4468 has a similar mineral composition and is similar in age to NWA1068 and LAR 06319, it is there for hypothesised that the NWA 4468 underwent a similar crystallization histories as the other two meteorites. NWA 4468 crystallization was not the result of magma mixing but rather the result of crystallization of olivines that where then entrained within the magma and then reintroduced at pyroxenes were crystallizing (Sarbadhikari et al., 2008 and Usui et al., 2008).

Chapter 6: Conclusion

6.1 Summary

Based on the textural and chemical analysis of NWA 4468 the following conclusions can be drawn about its cooling history.

(1) Pyroxenes crystallized at temperatures ranging from 1092°C to 1196°C. The Ca-rich and Ca-poor zoning suggests that pyroxene crystallization occurred in two stages.
(2) Olivine likely had two cooling events with early crystallization of olivine crystals occurring relatively quickly and incorporating chromite. Maximum temperatures of crystallization occurred in the range of 1402 °C to 1910 °C.
(3) The comparison between NWA 4468 other enriched shergottites of the similar age (NWA 1068 and LAR 06319) suggests the meteorites underwent similar crystallization histories. NWA 4468 likely underwent multiple stages of crystallization ,with the formation of olivine occurring before the crystallization of pyroxene. After olivine formed settled out of the melt before being entrained in upcoming magma where it was brought to lower pressures and temperatures in which pyroxene crystals were then formed.

Future work would include a LA-ICP-MS analysis of minor elements of pyroxene crystals and a full analysis of makyslonite to which could be used to determine temperatures of these minerals which would further expand of the knowledge of the crystallization of NWA 4468.

References

Agrell, S. O., Charnley, N. R., and Chinner, G. A. (1998). Phosphoran olivine from Pine Canyon, Piute Co., Utah. Mineralogical Magazine, 62(2), 265-269.

Aoki, K. I. (1964). Clinopyroxenes from alkaline rocks of Japan. American Mineralogist: Journal of Earth and Planetary Materials, 49(9-10), 1199-1223.

Barrat, J. A., A. Jambon, M. Bohn, Ph Gillet, V. Sautter, C. Göpel, M. Lesourd, & F. Keller. (2002) Petrology and chemistry of the picritic shergottite North West Africa 1068 (NWA 1068). Geochimica et Cosmochimica, 66(19), 3505-3518

Borg, L. E., & Draper, D. S. (2003). A petrogenetic model for the origin and compositional variation of the Martian basaltic meteorites. Meteoritics & Planetary Science, 38(12), 1713-1731.

Borg, L. E., Gaffney, A. M., & DePaolo, D. J. (2008, March). Preliminary age of martian meteorite Northwest Africa 4468 and its relationship to the other incompatible-element-enriched shergottites. In Lunar and Planetary Science Conference (Vol. 39, p. 1851).

Bouvier, A., Blichert-Toft, J., Vervoort, J. D., Gillet, P., and Albarède, F. (2008). The case for old basaltic shergottites. Earth and Planetary Science Letters, 266(1-2), 105-124.

Bussweiler, Y., Brey. G.P., Pearson, D.G., Stachel, T., Stern R.A., Hardman., M.F., Kjarsgaard, B.A. and Jackson, S.E. (2017). The aluminum-in-olivine thermometer for mantle peridotites – Experimental versus empirical calibration and potential applications. Lithos, 272, 301-314.

Chakraborty, S. (2010). Diffusion coefficients in olivine, wadsleyite and ringwoodite. Reviews in mineralogy and geochemistry, 72(1), 603-639.

Collinet, M., Médard, E., Charlier, B., Vander Auwera, J., & Grove, T. L. (2015). Melting of the primitive Martian mantle at 0.5–2.2 GPa and the origin of basalts and alkaline rocks on Mars. Earth and Planetary Science Letters, 427, 83-94.

Coogan, L. A., Saunders, A. D., & Wilson, R. N. (2014). Aluminum-in-olivine thermometry of primitive basalts: evidence of an anomalously hot mantle source for large igneous provinces. Chemical Geology, 368, 1-10.

De Hoog, J. C., Gall, L., Cornell, D. H., 2010. Trace-element geochemistry of mantle olivine and application to mantle petrogenesis and geothermobarometry. Chemical Geology, 270(1-4), 196-215.

Faure, F., Trolliard, G., Nicollet, C., Montel, J. M., 2003. A developmental model of olivine morphology as a function of the cooling rate and the degree of undercooling. Contributions to Mineralogy and Petrology, 145(2), 251-263.

Filiberto, J., 2017. Geochemistry of Martian basalts with constraints on magma genesis. Chemical Geology, 466, 1-14.

Goodrich, C.A., 2002. Olivine-phyric Martian basalts: A new type of shergottite. Meteroritics and Planetary Science, 37(S12), B31-B34.

Hartmann, W. K., Neukum, G., 2001. Cratering chronology and the evolution of Mars. Chronology and evolution of Mars pp. 165-194.

Hartmann, W.K., 2005. Martian cratering 8: Isochron refinement and the chronology of Mars. Icarus. 174(2), 294-320.

Irving, A. J., Kuehner, S. M., Korotev, R. L., Hupé, G. M., 2007. Petrology and bulk composition of primitive enriched olivine basaltic shergottite Northwest Africa 4468. In Lunar and Planetary Science Conference (Vol. 38, p. 1526).

Lapen, T. J., Righter, M., Brandon, A. D., Beard, B. L., Shafer, J., Irving, A. J., 2009. Lu-Hf isotope systematics of NWA4468 and NWA2990: Implications for the sources of shergottites. In Lunar and Planetary Science Conference (Vol. 40).

Lessel, J., Putirka, K., 2015. New thermobarometers for martian igneous rocks, and some implications for secular cooling on Mars. American Mineralogist, 100(10), 2163-2171.

Lissauer, J.J, Squyres, S.W., Hartmann, W.K., 1988. Bombardment History of the Saturn system. J.Geophys. Res. 93,13,776-13,804

McKenzie, D., Bickle, M. J., 1988. The volume and composition of melt generated by extension of the lithosphere. Journal of petrology, 29(3), 625-679.

Marks, E., Borg, L. E., Gaffney, A. M., DePaolo, D., 2010. The Relationship of northwest Africa 4468 to the other incompatible element-enriched shergottites inferred from its Rb-Sr and Sm-Nd isotopic systematics. Lunar Planet. Sci. XLI, 2064.

McSween Jr., H. Y, Treiman A.H., 1998. Martian samples. Papike, J.J. (Ed.), Planetry Materials: Reviews in Minerology, Mineralogical Scoiety America Vol. 36 pp. 6-1-6-53

McSween, H. Y., 1985. SNC meteorites: Clues to Martian petrologic evolution?. Reviews of Geophysics, 23(4), 391-416.

Milman-Barris, M. S., Beckett, J. R., Baker, M. B., Hofmann, A. E., Morgan, Z., Crowley, M. R., Vielzeuf, D., Stolper, E., Stolper, E., 2008. Zoning of phosphorus in igneous olivine. Contributions to Mineralogy and Petrology, 155(6), 739-765.

Nyquist, L.E., Wooden, J., Bansal, B., Wiesmann, H., McKay, G., Bogard, D. D., 1979. Rb-Sr age of the Shergotty achondrite and implications of metamorphic resetting of isochron age. Geochimica et Cosmochimica Acts, 43(7), 1057-1074.

Papike, J.J., Karner, J.M., Shearer, C.K., Burger, P.K., 2009. Silicate mineralogy of Martian meteorites. Geochimica et Cosmochimica Acta, 73(24), 7443-7485.

Sarbadhikari, A.B., Day, J M., Liu, Y., Rumble III, D., Taylore, L.A., 2009. Petrogenesis of olivine-phyric shergottite Larkman Nunatak 06319: Implications for enriched components in martian basalts. Geochimica et Cosmochimica Acta, 73(7), 2190-2214.

Shafer, J. T., Brandon, A. D., Lapen, T. J., Righter, M., Peslier, A. H., Beard, B. L., 2010. Trace element systematics and 147Sm–143Nd and 176Lu–176Hf ages of Larkman Nunatak 06319: Closed-system fractional crystallization of an enriched shergottite magma. Geochimica et Cosmochimica Acta, 74(24), 7307-7328.

Shih, C. Y., Nyquist, L. E., Reese, Y., Misawa, K., 2011. Sm–Nd and Rb–Sr studies of lherzolitic shergottite Yamato 984028. Polar Science, 4(4), 515-529.

Stöffler, D., Ryder, G., 2001. Stratigraphy and isotope ages of lunar geologic units: Chronological standard for the inner solar system. In Chronology and evolution of Mars (pp. 9-54). Springer, Dordrecht.

Symes, S. J., Borg, L. E., Shearer, C. K., Irving, A. J., 2008. The age of the Martian meteorite Northwest Africa 1195 and the differentiation history of the shergottites. Geochimica et Cosmochimica Acta, 72(6), 1696-1710.systematics. Lunar Planet. Sci. XLI, 2064.

Tanaka, K. L., 1986. The stratigraphy of Mars. Journal of Geophysical Research: Solid Earth, 91(B13).

Treiman, A. H., Gleason, J. D., Bogard, D. D., 2000. The SNC meteorites are from Mars. Planetary and Space Science, 48(12-14), 1213-1230.

Usui T., McSween H. Y., Floss C., 2008. Petrogenesis of olivine-phyric shergottite Yamato 980459, revisited. Geochim. Cosmochim, 72(6), 1711–1730

Vaucher J., Baratoux, D., Mangold, N., Pinet P, Kurita, K., Gregoire M., 2009. The volcanic history of central Elysium Planitia: implications of martian magmatism. Icarus, 204(2) 418-442.

Watson, E. B., Cherniak, D. J., Holycross, M. E., 2015. Diffusion of phosphorus in olivine and molten basalt. American Mineralogist, 100(10), 2053-2065

Appendix A

Backscattering Images

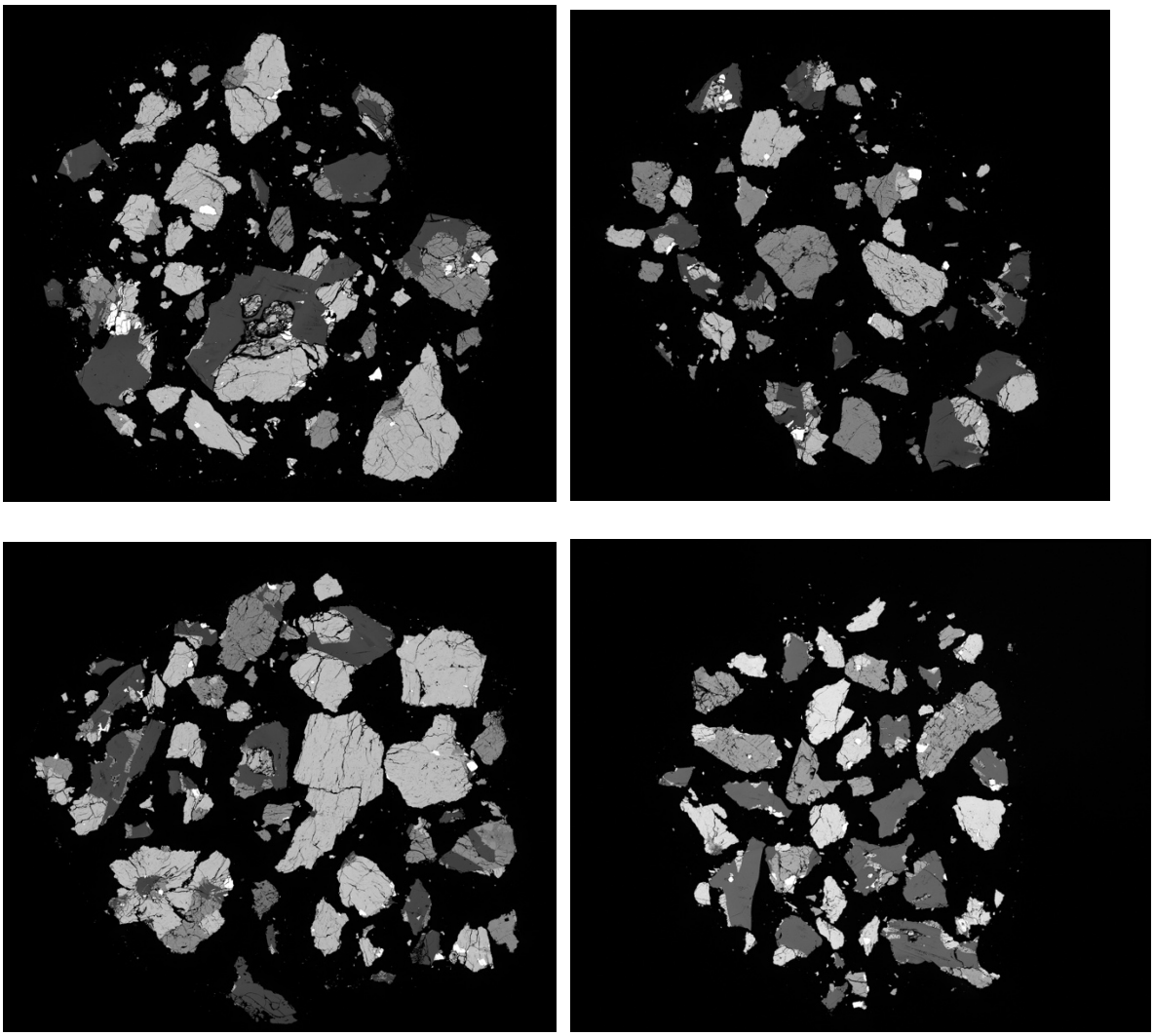

Microprobe X-ray maps

Pyroxene

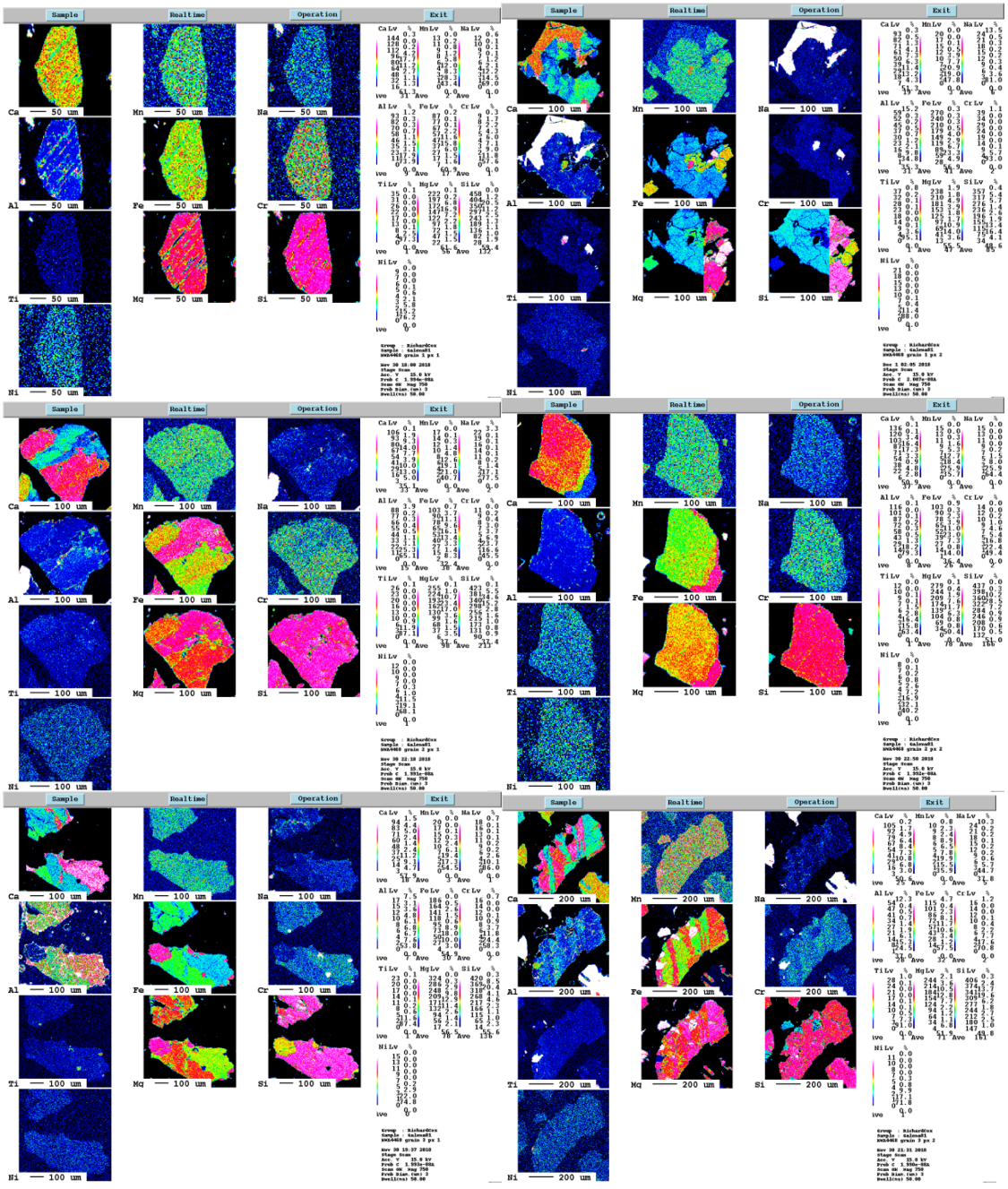

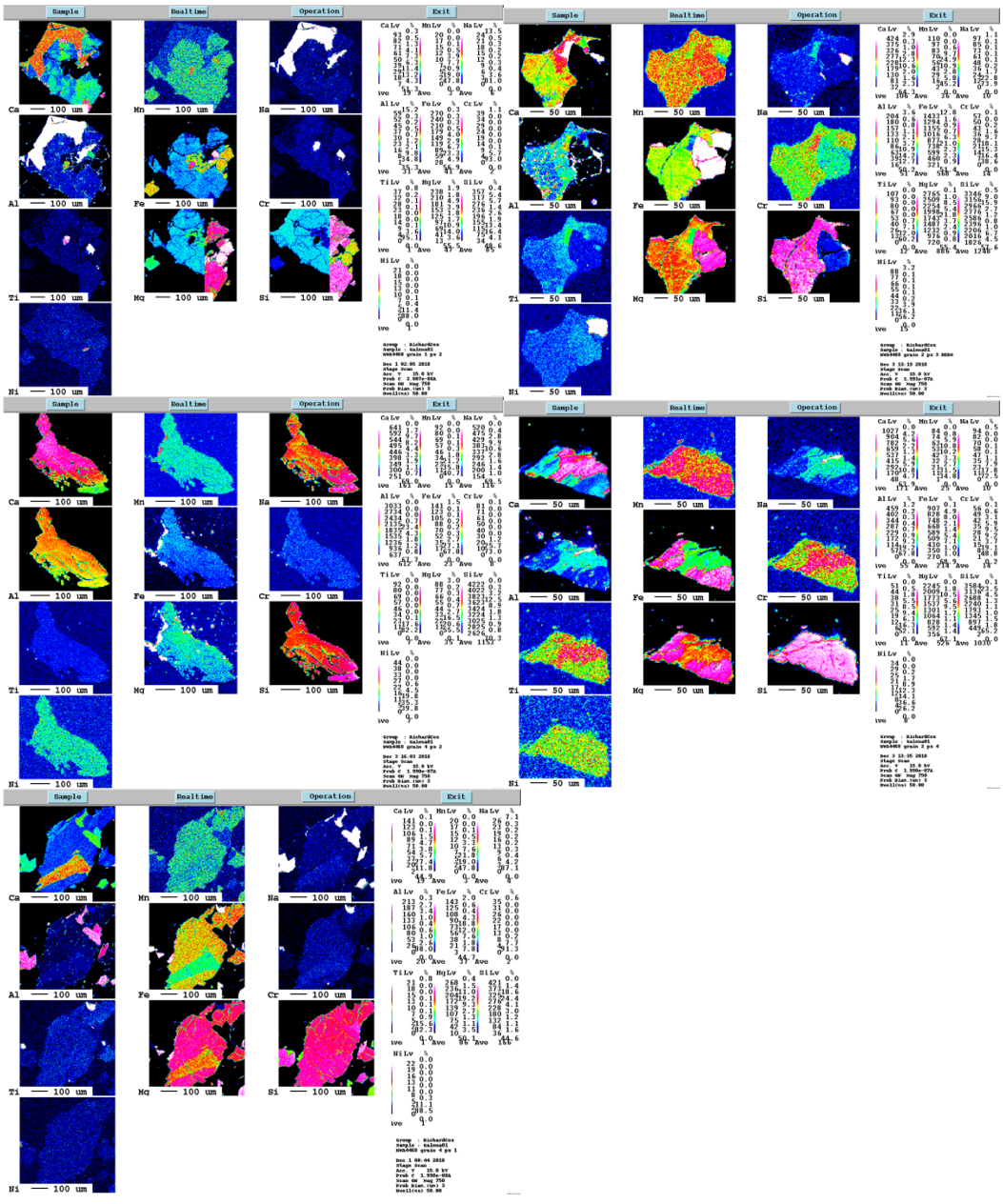
Sample
Realtime
Operation
Exit
Ca — 100 um
Mn — 100 um
Na — 100 um
Al — 100 um
Fe — 100 um
Cr — 100 um
Ti — 100 um
Mg — 100 um
Si — 100 um
Ni — 100 um
Ca — 50 um
Mn — 50 um
Na — 50 um
Al — 50 um
Fe — 50 um
Cr — 50 um
Ti — 50 um
Mg — 50 um
Si — 50 um
Ni — 50 um

Olivine

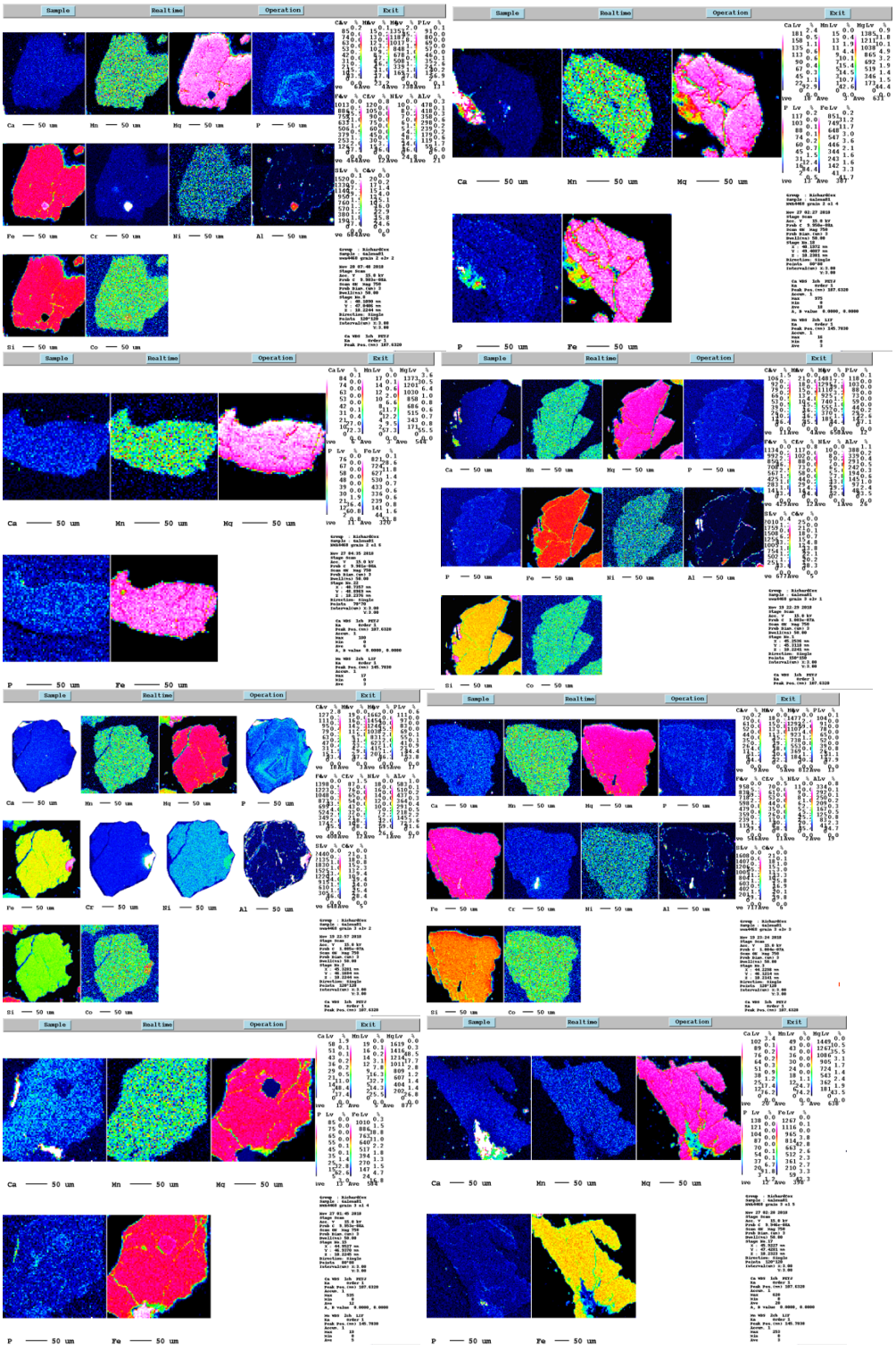

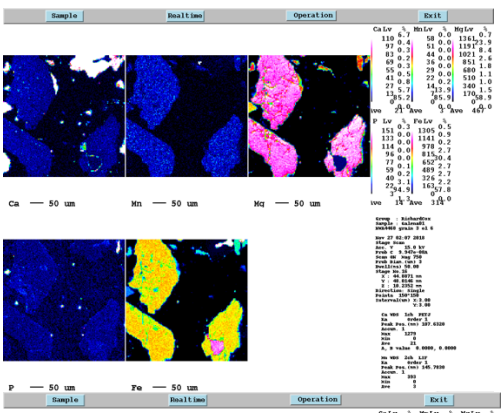
Sample
Realtime
Operation
Exit
Ca — 50 um
Mn — 50 um
Mg — 50 um
P — 50 um
Fe — 50 um

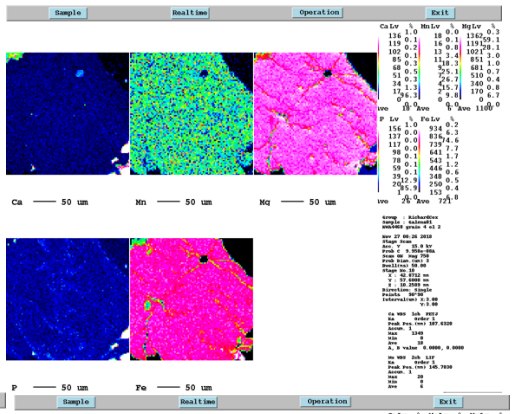
Sample
Realtime
Operation
Exit
Ca — 50 um
Mn — 50 um
Mg — 50 um
P — 50 um
Fe — 50 um

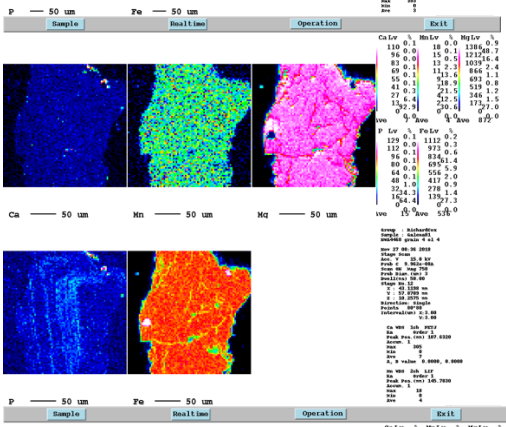
Sample
Realtime
Operation
Exit
Ca — 50 um
Mn — 50 um
Mg — 50 um
P — 50 um
Fe — 50 um

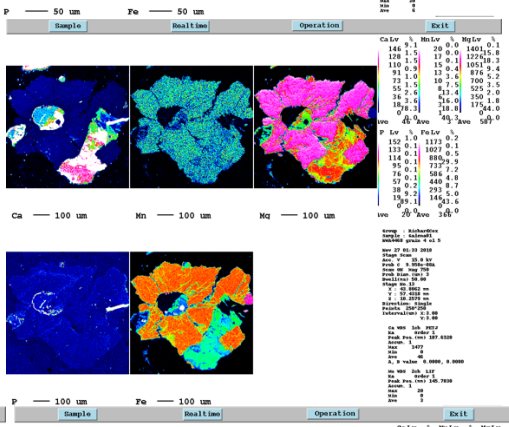
Sample
Realtime
Operation
Exit
Ca — 100 um
Mn — 100 um
Mg — 100 um
P — 100 um
Fe — 100 um

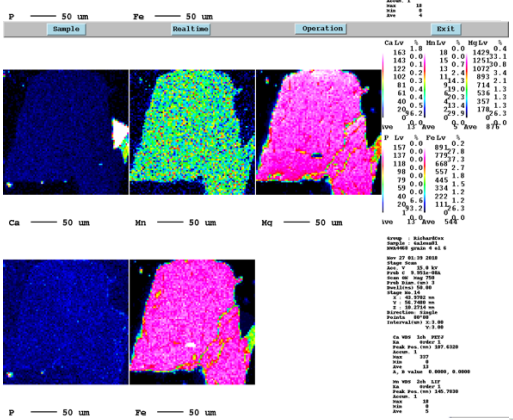
Sample
Realtime
Operation
Exit
Ca — 50 um
Mn — 50 um
Mg — 50 um
P — 50 um
Fe — 50 um

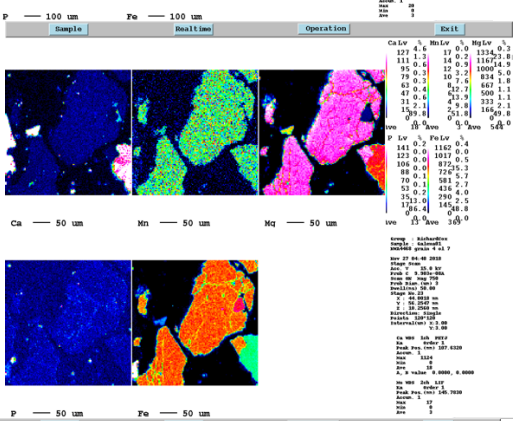
Sample
Realtime
Operation
Exit
Ca — 50 um
Mn — 50 um
Mg — 50 um
P — 50 um
Fe — 50 um

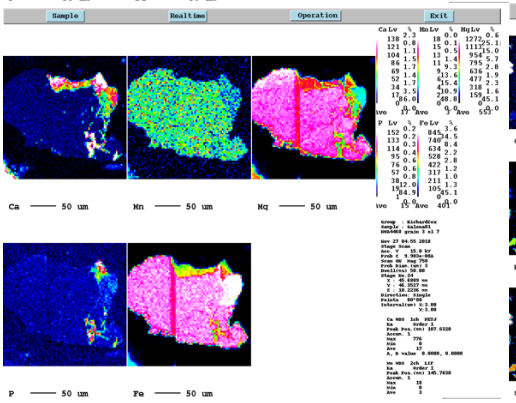
Sample
Realtime
Operation
Exit
Ca — 50 um
Mn — 50 um
Mg — 50 um
P — 50 um
Fe — 50 um

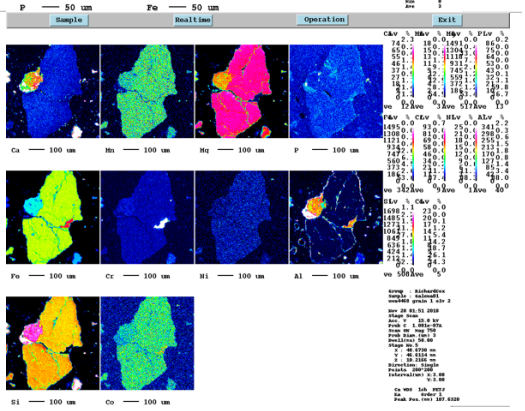
Sample
Realtime
Operation
Exit
Ca — 100 um
Mn — 100 um
Mg — 100 um
P — 100 um
Fe — 100 um
Cr — 100 um
Ni — 100 um
Al — 100 um
Si — 100 um
Co — 100 um

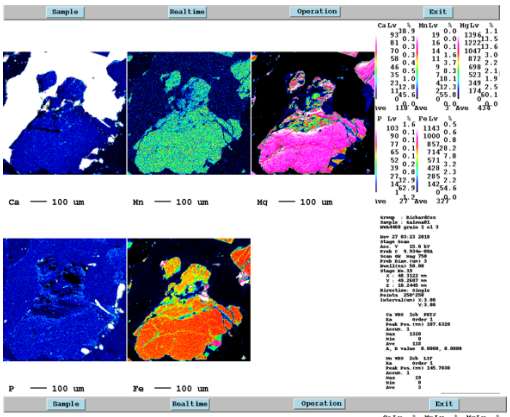
Sample
Realtime
Operation
Exit
Ca ── 100 um
Mn ── 100 um
Mg ── 100 um
P ── 100 um
Fe ── 100 um

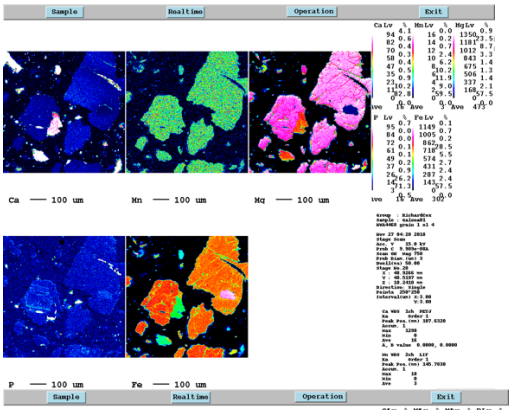
Sample
Realtime
Operation
Exit
Ca ── 100 um
Mn ── 100 um
Mg ── 100 um
P ── 100 um
Fe ── 100 um

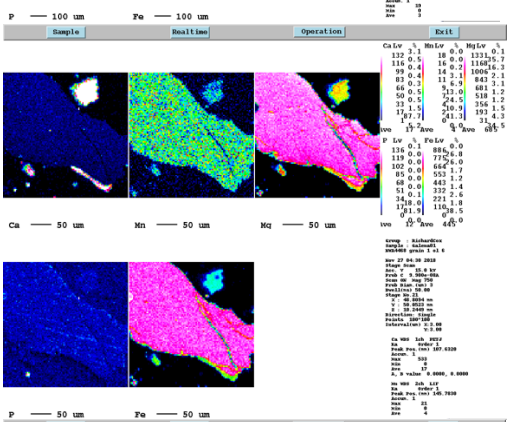
Sample
Realtime
Operation
Exit
Ca ── 50 um
Mn ── 50 um
Mg ── 50 um
P ── 50 um
Fe ── 50 um

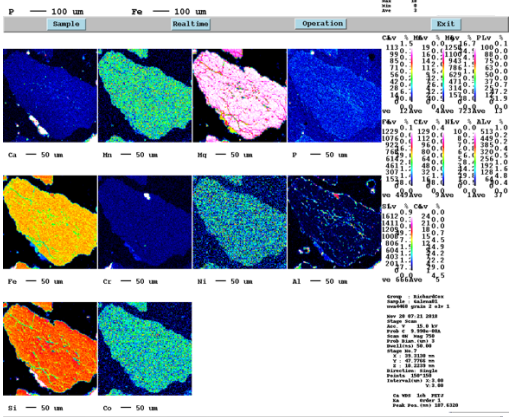
Sample
Realtime
Operation
Exit
Ca ── 50 um
Mn ── 50 um
Mg ── 50 um
P ── 50 um
Fe ── 50 um
Cr ── 50 um
Ni ── 50 um
Al ── 50 um
Si ── 50 um
Co ── 50 um

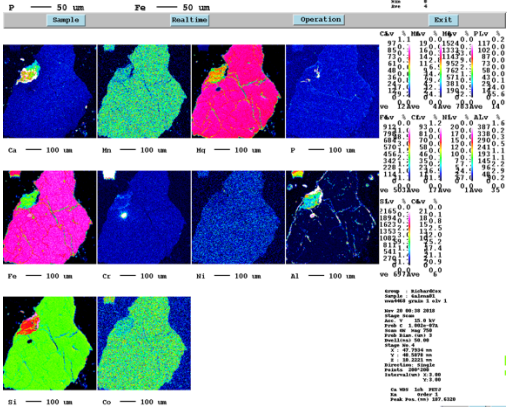
Sample
Realtime
Operation
Exit
Ca ── 100 um
Mn ── 100 um
Mg ── 100 um
P ── 100 um
Fe ── 100 um
Cr ── 100 um
Ni ── 100 um
Al ── 100 um
Si ── 100 um
Co ── 100 um

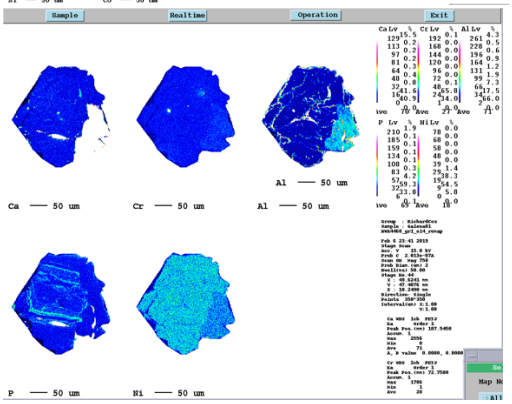
Sample
Realtime
Operation
Exit
Ca ── 50 um
Cr ── 50 um
Al ── 50 um
P ── 50 um
Ni ── 50 um

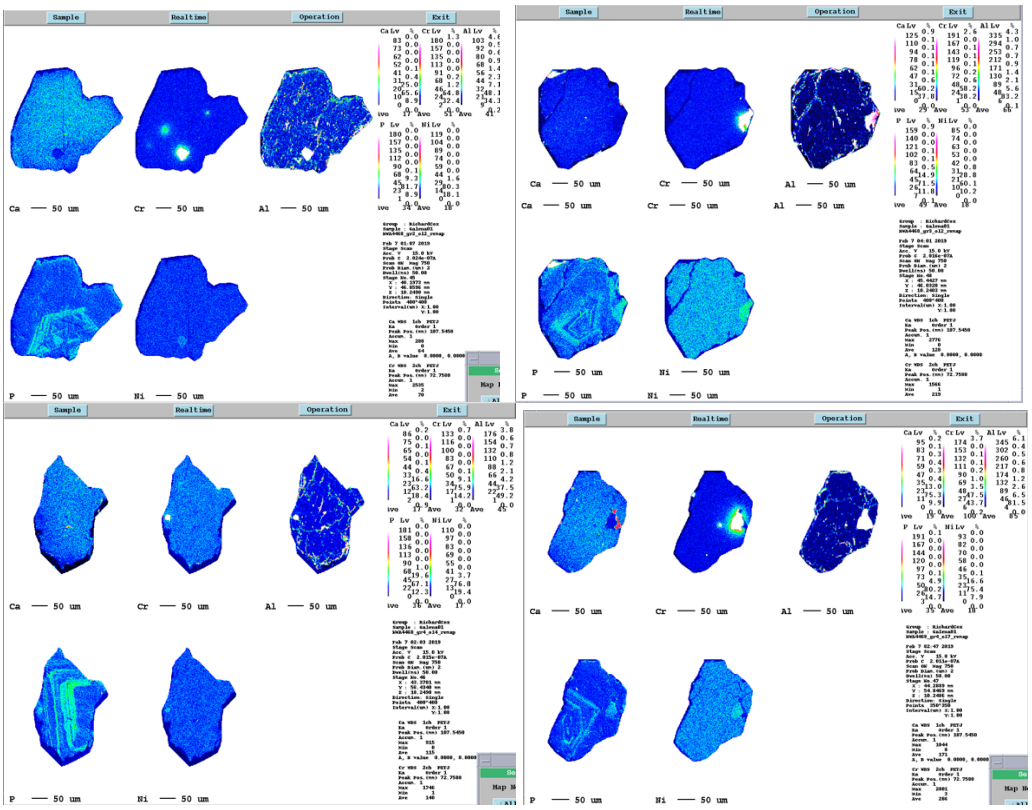

Appendix B

Please refer to the attached excel sheet for the complete list of raw data collected from the microprobe and LA-ICP-MS.